

Non-Darcy effects in fracture flows of a yield stress fluid

A. Roustaei¹, T. Chevalier², L. Talon^{2,†} and I. A. Frigaard^{1,3}

¹Department of Mechanical Engineering, University of British Columbia, 6250 Applied Science Lane, Vancouver, BC V6T 1Z4, Canada

²Laboratoire FAST, Univ. Paris-Sud, CNRS, Université Paris-Saclay, F-91405, Orsay, France

³Department of Mathematics, University of British Columbia, 1984 Mathematics Road, Vancouver, BC V6T 1Z2, Canada

(Received 4 December 2015; revised 15 July 2016; accepted 20 July 2016;
first published online 16 September 2016)

We study non-inertial flows of single-phase yield stress fluids along uneven/rough-walled channels, e.g. approximating a fracture, with two main objectives. First, we re-examine the usual approaches to providing a (nonlinear) Darcy-type flow law and show that significant errors arise due to self-selection of the flowing region/fouling of the walls. This is a new type of non-Darcy effect not previously explored in depth. Second, we study the details of flow as the limiting pressure gradient is approached, deriving approximate expressions for the limiting pressure gradient valid over a range of different geometries. Our approach is computational, solving the two-dimensional Stokes problem along the fracture, then upscaling. The computations also reveal interesting features of the flow for more complex fracture geometries, providing hints about how to extend Darcy-type approaches effectively.

Key words: lubrication theory, plastic materials, porous media

1. Introduction

Many complex fluids used in industrial applications exhibit yield stress behaviour, e.g. polymers, colloidal suspensions, foams, cement slurries, paints, muds, etc. (see Coussot 2005). Flows of these fluids are actively studied from theoretical, rheological and experimental perspectives (e.g. Balmforth, Frigaard & Ovarlez 2014; Coussot 2014). This paper addresses the non-inertial flow of single-phase yield stress fluids along uneven/rough-walled (two-dimensional) channels, e.g. approximating a fracture; see figure 1(a). Our paper has two main objectives. First, we wish to re-examine the usual approaches to providing a (nonlinear) Darcy-type flow law, and to show that such approaches may contain serious quantitative errors when yield stress fluid flows are considered, due to self-selection of the flowing region. Second, we aim to explore the details of the flow as the limiting pressure gradient is approached, showing that determination of the critical pressure gradient (or yield stress) for flow is non-trivial,

† Email address for correspondence: talon@fast.u-psud.fr

but also tractable in some situations. In satisfying these objectives we also shed light on other complex features of yield stress fluid flows through these geometries.

Non-inertial flows of Newtonian fluids are governed by the Stokes equations. Porous media and fractures cover a wide range of extremely complex geometries, but the linearity inherent in the Newtonian constitutive law means that the flow rate and pressure gradient are linearly related, as captured in Darcy's law and observed experimentally. Mathematical study of Darcy-type flows, the development of closure models for permeability and the application to groundwater hydrology were all well advanced by the 1950s, as was an understanding of many limitations of Darcy's law, e.g. inertial flows; see, e.g., Scheidegger (1957). A general model for non-Darcy effects was proposed by Christianovich (1940), largely to extend mathematical analysis to such flows. Here, we are concerned with non-Darcy effects that arise due to the non-Newtonian character of the fluid.

The original motivation for much of this work stems from oil recovery. Different non-Newtonian effects were of primary interest in different world regions. The excellent review of Savins (1969), for example, covers shear-thinning and viscoelastic effects, as these were the additives being used for enhanced recovery in North America at the time, but does not mention yield stress effects. On the other hand, in the former USSR, heavy oils exhibiting viscoplastic behaviour were being extracted, and consequently the study of such fluids in porous media settings evolved there. Fibre-bundle or capillary-tube models of yield stress fluids flowing through a porous medium naturally lead to a limiting pressure gradient (LPG) which must be exceeded in order to flow. Thus, LPG generalizations of Darcy's law into nonlinear filtration/seepage have been suggested and studied since the early 1960s, e.g. Sultanov (1960), Entov (1967). Entov (1967) attributes the first usage of LPG models for oil applications to Mirzadzhanzade (1959). Mathematically analogous systems were in fact suggested earlier for water flowing through argillaceous rocks; i.e. the critical pressure acts on the pore space not the fluid. Early work concerning LPG flows is summarized in the text by Barenblatt, Entov & Ryzhik (1989) which contains further references.

Applications that involve flow along uneven channels are various. In hydraulic fracturing operations, some frac fluids used have a yield stress (designed in order to enhance proppant transport). At the end of hydraulic fracturing, the flowback phase attempts to clean the gelled fluids from the proppant-laden fracture. Sealants are routinely injected into brickwork to block the spread of moisture in old buildings (damp-proof courses). Cement injection into porous media is advocated as a means of sealing CO₂ storage reservoirs. Cement slurries and drilling fluids flow along uneven narrow eccentric annuli in the primary cementing process (see Nelson & Guillot 2006). In the squeeze cementing process, oil and gas wells are repaired by injecting cements and other fine suspensions into thin cracks. Rock grouting represents another similar process; see El Tani (2012). Injection of yield stress fluids has also been proposed as a potential method for porosimetry by Ambari *et al.* (1990).

Due to the length scale of flows, geometric uncertainty and/or the need for industrial simplicity, it is often the case that nonlinear filtration/seepage approaches are preferred to (Navier–)Stokes formulations for practical flow computations. Determination of a closure relationship between the flow rate and the applied pressure, in porous or fractured materials, is consequently of interest. One approach is to consider flow through packed beds or porous structures, either experimentally (Park, Hawley & Blanks 1973; Al-Fariss & Pinder 1987; Chase & Dachavijit 2003, 2005; Clain 2010; Chevalier *et al.* 2013a) or numerically (Balhoff & Thompson 2004; Bleyer & Coussot

2014). The flow laws developed typically conform to the LPG type. This type of experiment can also be simulated using pore-throat or similar macro-scale models of the porous medium. In such models, a pore network or lattice is connected by capillary tubes along which one-dimensional (1D) flows (or similar closures) are assumed (see Roux & Herrmann 1987; Sahimi 1995; Balhoff & Thompson 2004; Chen, Rossen & Yortsos 2005; Sochi & Blunt 2008; Balhoff *et al.* 2012; Talon & Bauer 2013; Talon *et al.* 2013; Chevalier & Talon 2015). Heterogeneity can be introduced into the network via local throat resistance or length, either systematically or stochastically. Since each flow path experiences different heterogeneous pore throats, their critical opening pressures are different. As a result, the disorder of the porous medium induces a hierarchy in the flow paths that open, leading to a non-trivial relationship between the flow rate and the applied pressure drop (see Talon *et al.* 2013; Chevalier & Talon 2015).

Other approaches to deriving (LPG) closure flow laws are mostly classical. In the so-called ‘fibre-bundle model’ (e.g. Chen *et al.* 2005; de Castro *et al.* 2014), the homogeneous porous medium is considered as a succession of parallel tubes, each with a uniform cross-sectional area. The flow law is easily derived in each throat and the critical pressure is known. The major drawback is, of course, that it neglects the influence of heterogeneity along each flow path. For two-dimensional (2D) fractures/fissures/channels the most classical approach is to assume a lubrication or Hele-Shaw approximation, e.g. Ge (1997), Drazer & Koplík (2000), Malevich, Mityushev & Adler (2006); i.e. the mean flow is driven by a uniform pressure gradient along the varying gap. This approach has long been exploited in the modelling of laminar primary cementing flows, e.g. Bittleston, Ferguson & Frigaard (2002), Pelipenko & Frigaard (2004). After some algebra involving the solution of the Buckingham–Reiner equation, the flow rate can be related to the local width of the gap (inducing heterogeneity). In a single rough channel, Talon, Auradou & Hansen (2014) show that the critical pressure is proportional to the harmonic mean of the gap width, and the flow–pressure relationship is related to a series of power means. In non-uniform Hele-Shaw geometries, the critical pressure is locally defined and the fluid flows preferentially (similarly to pore-throat network approaches). For example, in the eccentric annular cementing flows of Bittleston *et al.* (2002) and Pelipenko & Frigaard (2004), the widest part of the annulus can flow while the narrowest part is stationary.

In this paper, we look at the effects of heterogeneity along a single channel (assumed to be 2D). We use accurate computations to solve the Stokes flow of a Bingham fluid flowing along complex fracture-like geometries and analyse the results to draw quantitative and qualitative conclusions useful for more general LPG-style closures. While the Hele-Shaw/lubrication approach (or indeed a fibre-bundle approach) can be straightforwardly applied to randomized varying gap widths, it has long been recognized that to do so may result in significant error where yield stress fluids are concerned. First of all, one faces the usual geometric restrictions of slow geometric variation which are likely to be invalid for many fractures. Second, the use of Hele-Shaw/lubrication scaling arguments needs careful attention (Walton & Bittleston 1991; Balmforth & Craster 1999; Putz, Frigaard & Martinez 2009), and the leading-order stress fields exhibit an $O(1)$ deviation from those of the naïve Hele-Shaw/lubrication approach. These errors arise from extensional stresses within the central plug, causing it to yield for modest heterogeneities (see Frigaard & Ryan 2004; Putz *et al.* 2009).

Larger-amplitude heterogeneity leads to the emergence of so-called ‘fouling layers’ at the walls of the duct, in which residual fluid is held stationary by the

yield stress. This geometric effect has been observed in various experimental and computational/analytical studies (de Souza Mendes *et al.* 2007; Chevalier *et al.* 2013b; Roustaei & Frigaard 2013; Bleyer & Coussot 2014; Roustaei, Gosselin & Frigaard 2015). Roustaei & Frigaard (2013) demonstrate that as the heterogeneity amplitude increases at fixed yield stress, fouling occurs beyond a critical amplitude, and give an empirical prediction for the onset of fouling. Such predictions are, however, strongly dependent on the specific geometry; e.g. in the abrupt expansion of de Souza Mendes *et al.* (2007), fouling occurs first in the corners, whereas for the smooth geometries of Roustaei & Frigaard (2013), fouling is first found in the deepest part of the channel. The most important result, from the perspective of predicting flow-rate–pressure-drop relationships, is that fouling results in self-selection of an $O(1)$ variation of the flowing geometry (Roustaei *et al.* 2015), which should therefore have an $O(1)$ effect on such relationships. Such phenomena have not been systematically studied from the perspective of flow rate–pressure drop, as we do here.

Second, we have the objective of understanding and quantifying the flow onset problem; i.e. in a given section of an uneven fracture, what is the critical pressure drop at which the fluid begins to flow? Although having a porous media flow objective, the methods we use focus on solving Stokes equations. The fracture geometry defines the flow (uniquely for given physical parameters) and hence the flow onset or limiting pressure drop. However, the reverse is not true, as shown nicely by Balhoff & Thompson (2004), i.e. the same limiting pressure drops are found for different geometries. For non-Newtonian fluids the geometry and rheology are closely coupled in determining a closure law. Use of multi-dimensional flow simulation is an essential tool for uncovering localized flow features which explain physical results that appear to be non-intuitive, e.g. as in Bleyer & Coussot (2014).

The plan of the paper is as follows. In §2, we present the model problem and fracture geometries that we consider in this paper, scale the corresponding equations, give an overview of the computational method and present example results. This is followed in §3 by a systematic comparison of the flow-rate–pressure-drop relationships from the computations with those from a naïve lubrication approximation, including some methods to improve the approximations in the situation where fouling occurs. Section 4 focuses on analysis of the critical limit of zero flow, from both the mathematical and computational perspectives. This is largely focused on characterizing the limiting flows in simple fracture geometries, although insights are also gained from these results for more complicated and realistic fractures. The paper closes with a discussion of the main results and future directions.

2. Model set-up

Figure 1 shows the flow geometry and notation used in the current study. We assume a fracture of nominal minimal width $2\hat{D}$, with walls located at $\hat{y} = \pm[\hat{D} + \hat{Y}_{\pm}(\hat{x})]$, where $0 \leq \hat{Y}_{\pm}(\hat{x}) \leq \hat{H}$. Both walls and the flow are assumed to be periodic in \hat{x} with period \hat{L} . The periodic fracture cell is assumed to be filled with a yield stress fluid (assumed to be a Bingham fluid for simplicity), which is flowing non-inertially. As we wish to understand how Darcy-law-type behaviour is modified geometrically and rheologically, we are interested in the mapping from flow rate (mean velocity) to pressure drop (and *vice versa*).

In a fracture of varying width the areal flow rate \hat{Q} is constant and the pressure gradient varies along the flow direction. Therefore, an imposed flow formulation will be adopted. To make the Stokes equations dimensionless we use \hat{D} as the length scale.

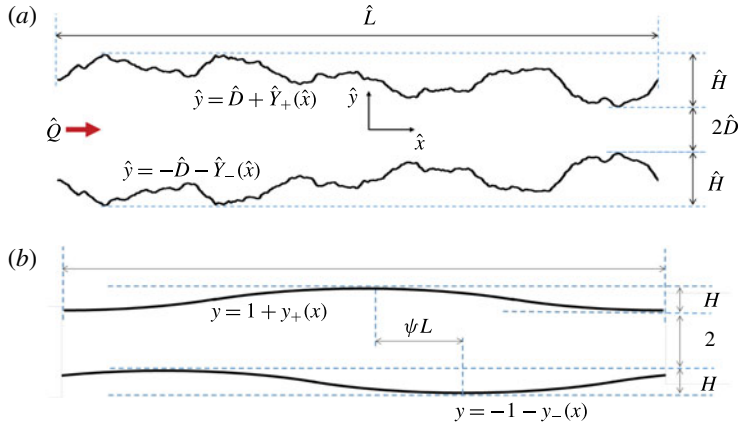


FIGURE 1. (Colour online) (a) Schematic of the 2D fracture showing the dimensional parameters; (b) schematic of the wavy-walled dimensionless geometry, with the lower wall shifted to the right by ψL .

Let \hat{U}_0 denote the mean velocity along the fracture, defined at the minimum fracture width, i.e. $\hat{U}_0 = \hat{Q}/2\hat{D}$. We use \hat{U}_0 to scale the velocity. The shear stresses are then scaled with $\hat{\mu}\hat{U}_0/\hat{D}$, where $\hat{\mu}$ is the plastic viscosity of the Bingham fluid. Any static pressure component is subtracted from the pressure, before also scaling with $\hat{\mu}\hat{U}_0/\hat{D}$. In the remainder of the paper, we consistently use the ‘hat’ symbol to denote variables that are dimensional, e.g. \hat{x} , and dimensionless variables are denoted without a hat, e.g. x . The dimensionless Stokes equations are

$$0 = -\frac{\partial p}{\partial x} + \frac{\partial}{\partial x}\tau_{xx} + \frac{\partial}{\partial y}\tau_{xy}, \tag{2.1}$$

$$0 = -\frac{\partial p}{\partial y} + \frac{\partial}{\partial x}\tau_{yx} + \frac{\partial}{\partial y}\tau_{yy}, \tag{2.2}$$

$$0 = \frac{\partial u}{\partial x} + \frac{\partial v}{\partial y}, \tag{2.3}$$

where $\mathbf{u} = (u, v)$ is the velocity, p is the modified pressure and τ_{ij} is the deviatoric stress tensor. The scaled constitutive laws are

$$\tau_{ij} = \left(1 + \frac{B}{\dot{\gamma}(\mathbf{u})}\right) \dot{\gamma}_{ij} \iff \tau > B, \tag{2.4a}$$

$$\dot{\gamma}_{ij}(\mathbf{u}) = 0 \iff \tau \leq B, \tag{2.4b}$$

where

$$\dot{\gamma}_{ij}(\mathbf{u}) = \frac{\partial u_i}{\partial x_j} + \frac{\partial u_j}{\partial x_i}, \quad \mathbf{u} = (u, v) = (u_1, u_2), \quad \mathbf{x} = (x, y) = (x_1, x_2), \tag{2.4c}$$

and $\dot{\gamma}$, τ are the norms of $\dot{\gamma}_{ij}$, τ_{ij} , defined as

$$\dot{\gamma} = \sqrt{\frac{1}{2} \sum_{ij} \dot{\gamma}_{ij}^2} \quad \text{and} \quad \tau = \sqrt{\frac{1}{2} \sum_{ij} \tau_{ij}^2}. \tag{2.5a,b}$$

A single dimensionless number appears above, the Bingham number, B ,

$$B \equiv \frac{\hat{\tau}_Y \hat{D}}{\hat{\mu} \hat{U}_0}, \tag{2.6}$$

which represents the competition between the yield stress $\hat{\tau}_Y$ and the viscous stresses. Two other geometric groups characterize the fracture shape: the dimensionless length $L = \hat{L}/\hat{D}$ and the maximal out of gauge depth $H = \hat{H}/\hat{D}$; see figure 1.

No-slip conditions are satisfied at the upper and lower walls:

$$\mathbf{u} = 0, \text{ at } y = 1 + y_+(x) \text{ and } y = -1 - y_-(x), \tag{2.7}$$

where $y_{\pm}(x) = \hat{Y}_{\pm}(\hat{x})/\hat{D}$. At the ends of the fracture we impose periodicity:

$$\left. \begin{aligned} \mathbf{u}(-L/2, y) &= \mathbf{u}(L/2, y), & \tau_{ij}(-L/2, y) &= \tau_{ij}(L/2, y), \\ p(-L/2, y) &= p(L/2, y) + \Delta p, \end{aligned} \right\} \tag{2.8}$$

$$2 = \int_{-1-y_-(x)}^{1+y_+(x)} u_1(x, y) dy. \tag{2.9}$$

Here, Δp denotes the frictional pressure drop, which is part of the solution and is determined by satisfying the flow rate constraint (2.9).

2.1. Fracture geometries

The dimensionless fracture wall shapes $y_{\pm}(x)$ satisfy the bounds $0 \leq y_{\pm}(x) \leq H = \hat{H}/\hat{D}$. We consider two generic simplified fracture geometries (sinusoidal walls and triangular walls) and a more complex affine geometry. An example affine geometry is shown schematically in figure 1(a) and the sinusoidal wavy fracture in figure 1(b). The sinusoidal fracture widths are given by

$$y_+(x) = \frac{H}{2} [1 + \cos(2\pi x/L)], \quad y_-(x) = \frac{H}{2} [1 + \cos(2\pi[x/L - \psi])], \tag{2.10a,b}$$

with $\psi \in [0, 1]$ denoting a phase shift of the lower wall relative to the upper one, i.e. the lower wall is translated ψL to the right. The triangular geometry is defined analogously.

In many applications, it has been observed that fracture roughness may display self-affine correlations (Mandelbrot, Passoja & Paullay 1984; Schmittbuhl, Gentier & Roux 1993; Bouchaud 1997). A surface $\hat{y}(\hat{x})$ is self-affine if the probability to find the increment $\Delta\hat{y}$ after a distance $\Delta\hat{x}$ displays the scaling invariance

$$p(\Delta\hat{y}, \Delta\hat{x}) = \lambda^{\zeta} p(\lambda^{\zeta} \Delta\hat{y}, \lambda \Delta\hat{x}), \tag{2.11}$$

where λ is any scaling factor and ζ is called the Hurst exponent. An important property of self-affine surfaces is that all of the moments scale with the length of measurement as

$$M_n(\hat{x}) = (|\hat{y}(\hat{x} + \Delta\hat{x}) - \hat{y}(\hat{x})|^n)^{1/n} \propto |\Delta\hat{x}|^{\zeta}. \tag{2.12}$$

For the present paper, we have generated three types of fracture. In the first type, the two walls y_{\pm} are independently generated with a Hurst exponent $\zeta = 0.5$ using a Fourier transform method (see Sahimi 1995; Talon, Auradou & Hansen 2010). Both surfaces are scaled to have $\min y_{\pm} = 0$ and $\max y_{\pm} = H$. In the second type, we used $y_+ = y_-$. In the third type, we used $y_+ = -y_-$.

2.2. Computational overview

Numerical solution of viscoplastic fluids poses a unique challenge, which is the singularity of the effective viscosity in the constitutive equation (2.4), where $\dot{\boldsymbol{\gamma}} \rightarrow 0$ (unyielded regions). Aside from such points, the Bingham fluid is simply a generalized Non-Newtonian fluid with an effective viscosity $\mu = (1 + B/\dot{\boldsymbol{\gamma}})$. A common work around for the singular effective viscosity is to simply regularize the viscosity, introducing a small parameter $\epsilon \ll 1$, such that the effective viscosity scales like ϵ^{-1} as $\dot{\boldsymbol{\gamma}} \rightarrow 0$. Many such regularizations are possible. It can be shown that as $\epsilon \rightarrow 0$ the velocity solution will converge to that of the exact Bingham fluid, but the stress field may not; see Frigaard & Nouar (2005). Consequently, we may not infer the correct shape of the yield surface from $\tau = B$; e.g. Wang (1997).

Instead, we use the augmented Lagrangian (AL) method (Fortin & Glowinski 1983; Glowinski & Le Tallec 1989), which uses the proper variational formulation of the problem, as formulated, for example, by Duvaut & Lions (1976). The AL method introduces two new fields, the strain rate $\boldsymbol{\gamma}$ and stress \boldsymbol{T} , in addition to the velocity and pressure (\boldsymbol{u}, p) of the original problem. In this way, it relaxes the convex but non-differentiable velocity minimization problem to an associated saddle point problem. The saddle point problem is solved iteratively. Each iteration consists of three Uzawa split steps, to update (\boldsymbol{u}^n, p^n) , $\boldsymbol{\gamma}^n$ and \boldsymbol{T}^n . These iterations are repeated until $\max\{|\boldsymbol{\gamma}^n - \dot{\boldsymbol{\gamma}}^n|_{L^2}, |\boldsymbol{u}^n - \boldsymbol{u}^{n-1}|\} \leq 10^{-6}$ is satisfied or a maximum number of iterations (here 10 000) is reached. The $\boldsymbol{\gamma}$, \boldsymbol{T} fields of the AL method converge respectively to the strain rate and deviatoric stress tensors of the exact Bingham flow.

The AL approach is effectively a fixed-point iteration and suffers from slow convergence. In recent years, a number of authors have been working on improving the convergence speed; e.g. de los Reyes & González Andrade (2012), Treskatis, Moyers-Gonzalez & Price (2015) and Saramito (2016). While undoubtedly these approaches will come to fruition and common usage, familiarity with the AL approach and access to multiple CPUs has made the search for improved efficiency less urgent for the present study. We have implemented the AL method using the freely available FreeFEM++ finite element environment (Hecht 2012). Our algorithm is based on that of Saramito & Roquet (2001) with the addition of a flow rate constraint. To satisfy the inf-sup condition, Taylor-Hood (P_2 - P_1) elements are used for the velocity and pressure. Linear discontinuous elements $P_{1,d}$ are used for the $\boldsymbol{\gamma}$ and \boldsymbol{T} fields, to follow compatibility conditions between the velocity space and the strain/stress spaces. Both the velocity and the pressure are implicitly solved and the system matrix is factorized once for all iterations. To improve the accuracy of the solution while keeping reasonable runtime, five cycles of the anisotropic mesh adaptation (Borouchaki *et al.* 1997) are used.

A typical computation presented below starts with a size of 8000–10 000 mesh points. A new mesh is generated based on a metric computed from the current solution. We use the dissipation field as the metric, which results in a finer mesh around the yield surface. After the fifth cycle, the mesh may contain up to 150 000 mesh points, and the yield surfaces can be clearly identified by a much finer local mesh. The underlying combination of discretization and algorithm is analysed in Saramito & Roquet (2001), with various benchmarks computed. More details on the numerical algorithm specific to channel flows are described in Roustaei & Frigaard (2013) and Roustaei *et al.* (2015) and are skipped here for conciseness.

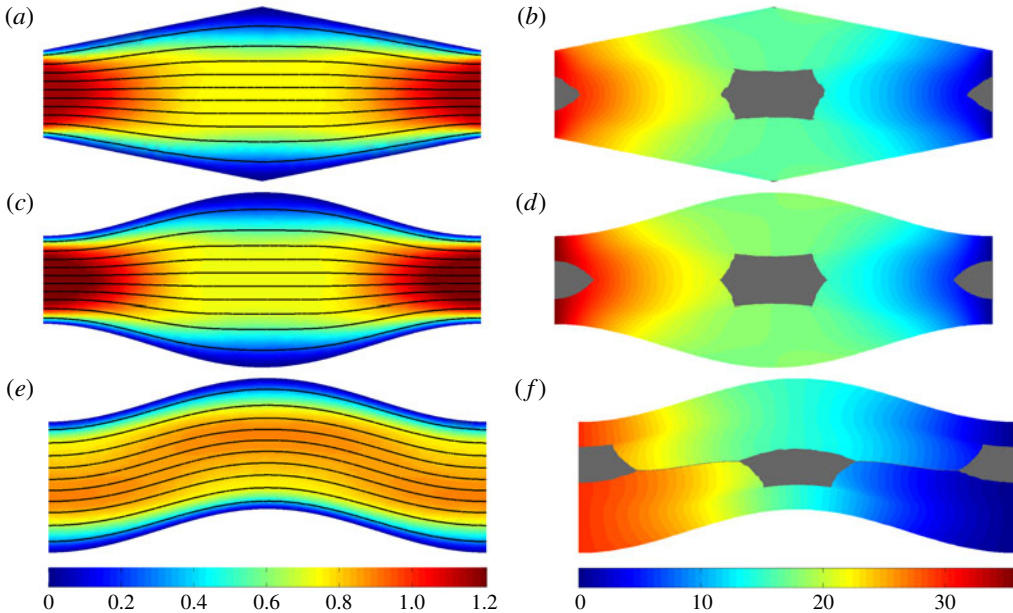


FIGURE 2. (Colour online) Computed examples of speed $|\mathbf{u}|$ and streamlines (a,c,e), and pressure p with (grey) unyielded plugs (b,d,f), at $H = 1$, $L = 10$, $B = 2$. (a,b) Triangular fracture profile, $\psi = 0$; (c,d) wavy fracture profile, $\psi = 0$; (e,f) wavy fracture profile, $\psi = 0.5$.

2.3. Example results

We have computed over 2000 flows, covering a wide range of H , L and B , for both triangular and wavy fracture profiles with different values of ψ . In addition, we have computed a smaller number of flows in affine fracture geometries. Before analysing specific features of the flow, we present some examples to illustrate qualitative features of our results.

Figure 2 shows results from a relatively modest fracture geometry and yield stress rheology ($H = 1$, $L = 10$, $B = 2$). Figure 2(a–d) shows the triangular and wavy profiles for $\psi = 0$ (symmetric fracture). The flow is evidently symmetric about the centreline and the widest part of the fracture. Unyielded plug regions are found at the symmetry points in x and close to the fracture centreline. There is very little difference, qualitatively or quantitatively, between triangular and wavy profiles. Figure 2(e,f) shows the wavy profile at $\psi = 0.5$, where the lower wall is out of phase with the upper wall. Here, the differences are quite significant. The velocity field appears to adapt smoothly to the wavy geometry, but no longer has the fastest fluid in the centre of each cross-section. Instead, the fastest travelling fluid moves at larger radius of curvature, while the plug regions are displaced into each bend. Due to symmetry effects, we observe a rather spectacular effect on the pressure field: the displaced central plug regions are joined by thin strands of unyielded fluid. It appears that the pressure is discontinuous across these strands, which is possible. It should be noted, however, that the traction vector, defined by the normal to these strands, is continuous.

Figure 3 explores the effects of increasing the yield stress on the flow of figure 2 ($H = 1$, $L = 10$, $\psi = 0$). The flow, of course, remains symmetric and, since the flow rate

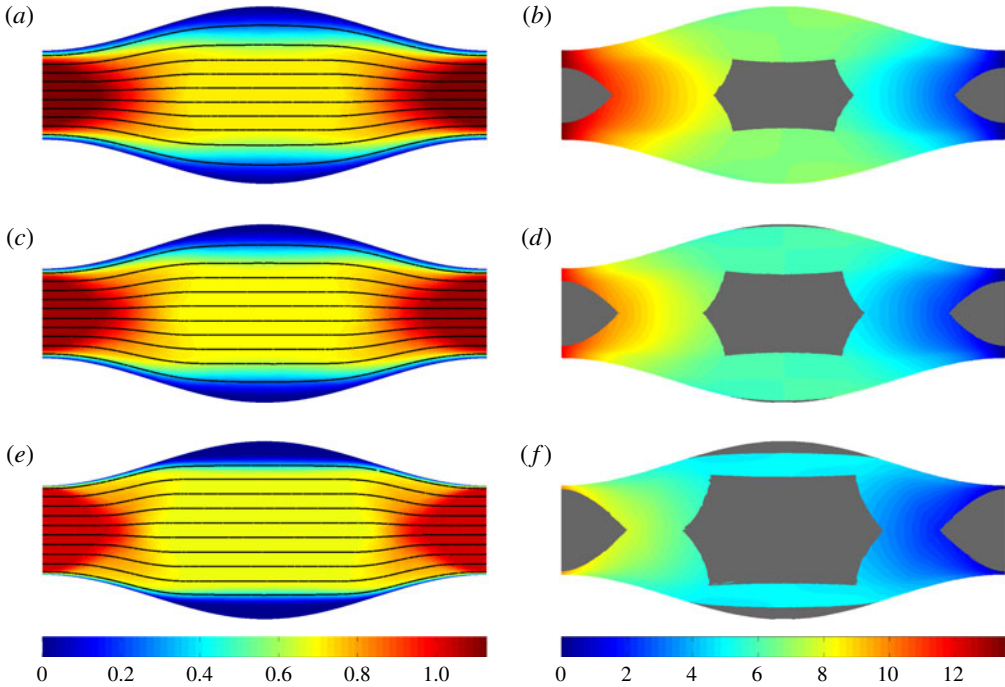


FIGURE 3. (Colour online) Computed examples of speed $|u|$ and streamlines (*a,c,e*), and scaled pressure p/B with (grey) unyielded plugs (*b,d,f*), at $H = 1$, $L = 10$, $\psi = 0$, wavy fracture profile; (*a,b*) $B = 5$, (*c,d*) $B = 10$, (*e,f*) $B = 100$.

is fixed, we only observe a relatively small change in the streamlines (figure 3*a,c,e*) as B is increased. This, however, masks the changes that are occurring in the pressure and stress fields. Increasing B results in a widening of the plugs in both narrow and wide parts of the fracture (figure 3*b,d,f*). The magnitude of the pressure field also increases with B : the flow rate is fixed and the pressure gradient therefore needs to overcome the yield stress everywhere along the fracture to ensure flow (hence p/B is shown to aid comparison). For $B \approx 10$ we observe that a region of stationary fluid emerges at the upper and lower walls, in the deepest part of the fracture. We refer to this as a fouling layer. The fouling layer grows in size as B increases. Growth of the fouling layer has effects on the pressure drop along the fracture and is an important part of the yield limit that is attained as $B \rightarrow \infty$, both of which are studied later; see § 4.

Figure 4 explores the effects of increasing H on the flow illustrated in figure 2(*e,f*) ($B = 2$, $L = 10$, $\psi = 0.5$). The flow asymmetry is preserved as H is increased, together with the interesting unyielded fluid strands. The main observation is that, although the yield stress is maintained constant, the region of fouled fluid in the deepest parts of the fracture increases markedly with H . The increase in fouling has the interesting effect of reducing the tortuosity of the flowing region of fluid. This self-selection of the flowing area is a unique effect of the yield stress.

Finally, we show an example from an affine fracture at $H = 2$, $L = 20$, for large B ; see figure 5. Even for $B = 1$, 10 (not shown), much of the small-scale roughness of the fracture wall is smoothed out by fouled immobile fluid. This effect increases with B as also the size of plug regions within the flowing region increases. Unyielded flowing plugs grow from various symmetry points of the geometry and at large B

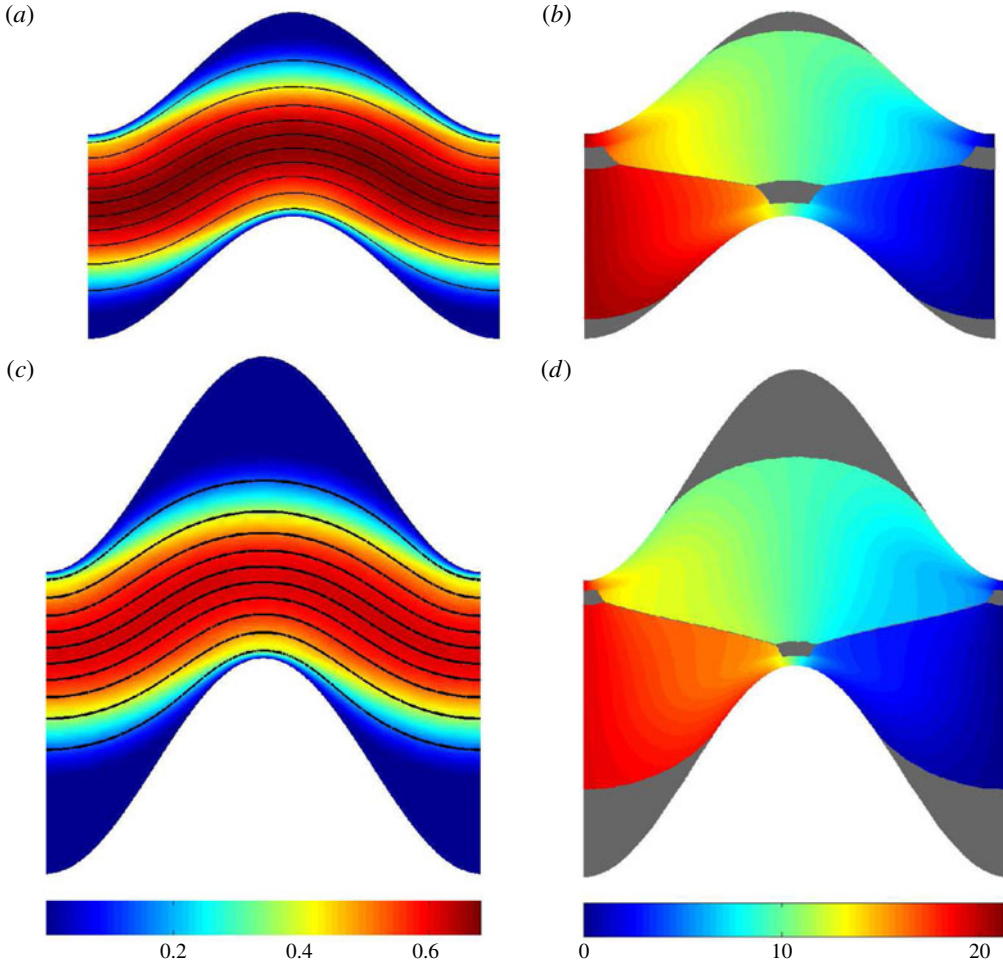


FIGURE 4. (Colour online) Computed examples of speed $|u|$ and streamlines (a,c), and pressure p with (grey) unyielded plugs (b,d), at $B = 2$, $L = 10$, $\psi = 0.5$, wavy fracture profile; (a,b) $H = 3$, (c,d) $H = 5$.

appear to approach the walls, leaving only thin shear layers. Some two-dimensional parts of the flow also appear to remain yielded at large B . For all practical purposes, the velocity field is symmetrical about the x -axis, but we can observe a slight asymmetry in the positions of plug regions. This asymmetry is due to the tolerance in the iteration and the unstructured mesh, which is not constrained to be symmetric. The AL approach iterates until a specified tolerance is achieved on velocity and strain rate. Plug regions are specified directly from the iteration on each element, which sets the strain rate to zero if the (iterated approximation to the) stress does not exceed the yield stress locally. Elements that are converging to zero strain rate may satisfy the convergence criterion by virtue of the strain rate being small. Thus, yield surface positions are determined by the element topology and consequently are less smooth than the analytical representation. The alternative method of regularizing the viscosity ensures a smooth contour, but the yield surface may be false as there is no guarantee of stress convergence.

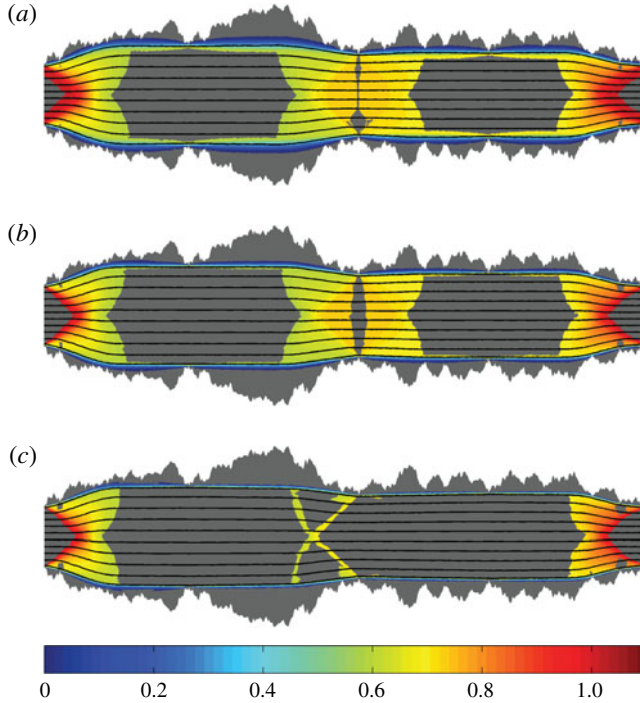


FIGURE 5. (Colour online) Computed examples of speed $|u|$ and streamlines for a symmetric affine fracture. The parameters are $H = 2$, $L = 20$, $B = 100, 1000, 10000$, from (a) to (c), with (grey) unyielded plugs.

3. Darcy-law estimates

In a uniform channel of dimensionless width $2(1 + h)$, the dimensionless pressure gradient is found from the constraint of fixed flow rate. This amounts to solving the Buckingham–Reiner equation:

$$1 = \frac{B(1 + h)^2}{3\phi} (1 - \phi)^2 (1 + \phi/2) \tag{3.1}$$

for the dimensionless parameter $\phi \in [0, 1]$, which denotes the ratio of yield stress to wall shear stress. We note that ϕ depends only on the parameter $B(1 + h)^2$, which can be interpreted as an appropriately modified Bingham number; i.e. the mean velocity is reduced by $1/(1 + h)$ due to mass conservation, and the minimal width is amplified by $(1 + h)$. Having found ϕ by solving (3.1) numerically, the pressure gradient is computed from

$$\left| \frac{\partial p}{\partial x} \right| = \frac{B}{(1 + h)\phi}. \tag{3.2}$$

In the case that the fracture has a slowly varying width in x , it is natural to expect that the uniform channel solution will give a leading-order approximation. The flow rate is the same at each x along the fracture, so we simply compute $\phi(x)$ from (3.1) using the varying width:

$$2(1 + h(x)) = 2 + y_+(x) + y_-(x), \quad \Rightarrow \quad h(x) = \frac{1}{2}[y_+(x) + y_-(x)]. \tag{3.3}$$

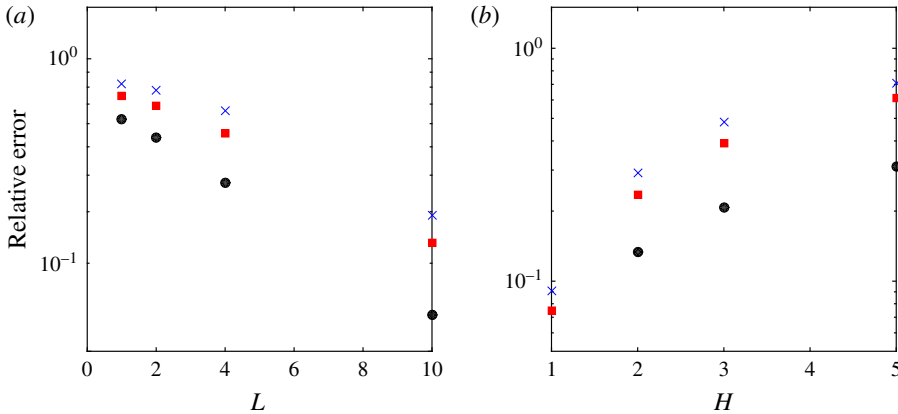


FIGURE 6. (Colour online) Relative error in predicted pressure drops between numerically computed values and the lubrication approximation (3.2), for $B=0.1$ in wavy fracture: (a) $H=2$ and varying L ; (b) $L=10$ and varying H . For both panels: black circle, $\psi = 0$; red square, $\psi = 0.25$; blue cross, $\psi = 0.5$.

We then evaluate the pressure gradient from (3.2). For example, for the wavy channel we have

$$h(x) = \frac{H}{4} [2 + \cos(2\pi x/L) + \cos(2\pi[x/L - \psi])]. \tag{3.4}$$

Adopting this procedure, we compute the lubrication theory pressure drop along the fracture Δp_L , using (3.1) and (3.2). The above procedure mimics that of constructing Darcy-law-type estimates from capillary-tube/fibre-bundle approaches and allowing slow variations in tube diameter. In the Newtonian setting, it leads to the usual Hele-Shaw analogy to the Darcy-flow law.

The estimate Δp_L may be compared directly with the numerical pressure drop Δp_N , from the finite element solution. We evaluate the accuracy of the lubrication approximation using the relative error in predicted pressure drops:

$$\text{Relative error} = \frac{|\Delta p_N - \Delta p_L|}{\Delta p_N}. \tag{3.5}$$

Figure 6 shows typical variations in relative error as both H and L are varied, for relatively small $B=0.1$. For this small value of B , the velocity field is very close to that of a Newtonian fluid, as are the relative errors in pressure drop. We observe that the relative error decreases for fixed H as L increases and for fixed L as H decreases. The relative errors appear to be largest for $\psi = 0.5$, when the sinusoidal wall variations are out of phase. This particular effect is due to tortuosity.

For Newtonian fluids, various authors have proposed corrections to Darcy’s law, based on improved representations of the geometric effects. For example, Zimmerman, Kumar & Bodvarsson (1991) have used an effective fracture width, derived by calibrating with the analytical solution from a sinusoidal variation. They have then generalized this approach somewhat to more general planar fractures. A slightly different approach is followed by Ge (1997), who essentially uses the fracture wall geometry to define a centreline of the fracture and consequently the local fracture width. This new fracture width is used in the classical lubrication approximation,

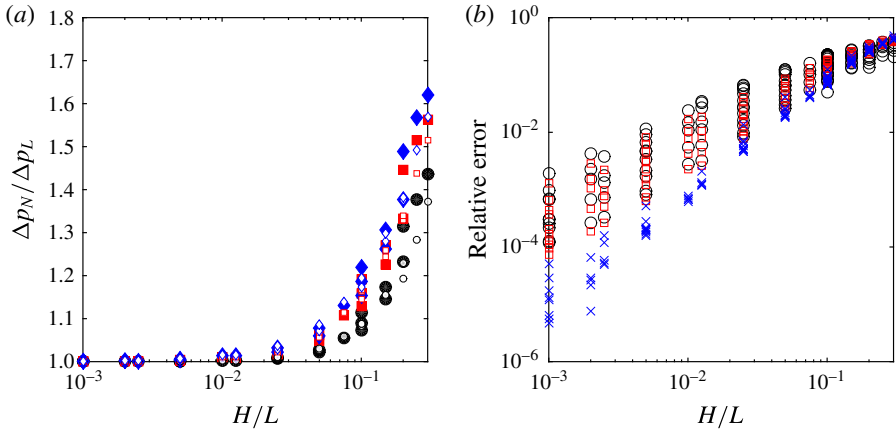


FIGURE 7. (Colour online) (a) Ratio of pressure drops computed numerically (Δp_N) and from the lubrication approximation (Δp_L): $B = 1$ (circles), $B = 5$ (squares), $B = 10$ (diamonds); filled symbols from triangular fracture profile, hollow symbols from wavy profile; $\psi = 0$. (b) Relative error in predicted pressure drops between numerically computed values and the lubrication approximation (3.2), for $L \geq 10$ and $B \geq 1$ in a wavy fracture: black circle, $\psi = 0$; red square, $\psi = 0.25$; blue cross, $\psi = 0.5$.

integrated along the fracture length. This approach does have the advantage of addressing tortuosity directly, i.e. the increase in flow path length, but is impractical in rough fractures as it relies on differentiating the fracture geometry. In general, we can say that the main efforts to correct geometric effects on Darcy's law for Newtonian fluids do not involve fluid rheology. This is for the simple reason that the geometry and rheology decouple for a Newtonian fluid, due to the linearity of the Stokes equations. We may infer from general continuity results as $B \rightarrow 0$ that any of these correction methods could be extended perturbatively into the weakly nonlinear regime of $0 < B \ll 1$; indeed, this is a relatively straightforward but laborious algebraic exercise.

We turn instead to moderate values of B . Figure 7(a) shows the ratio of pressure drops along the fracture, $\Delta p_N / \Delta p_L$, for $B = 1, 5, 10$ and at $\psi = 0$. Both wavy and triangular fracture shapes are plotted. We observe that the computed pressure drop exceeds the lubrication pressure drop. The ratio approaches 1 as $H/L \rightarrow 0$. It should be noted that multiple computations in our data set have the same values of H/L . Taking now $B \geq 1$ and $L \geq 10$, we plot in figure 7(b) the relative error for the wavy fracture, grouped by phase shift ψ . We observe that the relative errors are numerically of size $\sim H/L$ over all parameters. It should be noted that at the same ψ and H/L different data points correspond to different B . Interestingly, the smallest errors are found for $\psi = 0.5$, i.e. out of phase (reversing the trend at small B). Possibly this results from some form of cancellation of errors when averaged over a full wavelength (due to the phase shift). Analogous results are found for the triangular fracture profile. This leads us to suppose that for quite general geometries with $H/L \ll 1$, using (3.2) will give a reliable approximation to the pressure drop; roughly speaking, errors of 10% or less are found for $H/L < 0.05$.

We now explore a slightly different yield stress effect. We have seen in figure 3 that the flow domain may self-select. From our earlier work, e.g. Roustaei & Frigaard (2013), Roustaei *et al.* (2015), we expect to find this phenomenon for sufficiently large

H/L and B . The occurrence of a significant unyielded plug region in the deep parts of the fracture (called fouling layers) clearly changes the flow geometry, making this a non-Darcy-flow effect that is unique to yield stress fluids. In the case that we have fouling layers, the yield surface forms one boundary of the flow domain. This surface is defined as a contour of constant $\tau = B$, and is coincidentally a material surface when $\mathbf{u} = 0$ within the plug. Imposing the condition $\mathbf{u} = 0$ on the yield surface and solving only within the flowing region of the fracture gives the same velocity solution. This suggests that a reasonable way of approximating the pressure drop through such a fracture would be to replace $y_{\pm}(x)$ in (3.3) with the yield surface positions of the boundary of the fouling layer, denoted say $y = \pm y_{y,\pm}(x)$, i.e.

$$h(x) = \frac{1}{2}[\min\{y_+(x), y_{y,+}(x)\} + \min\{y_-(x), y_{y,-}(x)\}]. \tag{3.6}$$

To illustrate this approach, we take a fracture geometry $H=2$ and $L=2$, for which the lubrication approximation (3.2) should not provide a good approximation. The 2D computed mean pressure gradients and those approximated from (3.2) are shown in figure 8(a) for both triangular and wavy profiles, over $\psi = 0, 0.125, 0.25, 0.5$, and for increasing values of $B \geq 1$. Both mean pressure gradients increase with B , as might be expected, and we observe a consistent and significant error for all parameters. The relative error is shown in figure 8(b) for the same data (squares), and we see this is ~ 1 over all parameters. Also in figure 8(b) (diamonds) are the results of predicting the pressure drop using (3.2) but taking the modified fracture width from (3.6); i.e. where there is a fouling layer we take the yield surface position instead of the fracture wall position. Physically, as B increases the fouling layer progressively fills in and smoothes the fracture wall variations. Thus, as B increases, the geometry of (3.6) resembles a geometry more suited to a lubrication approximation. On using (3.6) we see a significant decrease in the relative error, so that at large B equation (3.2) again leads to a reasonable approximation of the pressure drop, but with the inconvenient caveat that we must first know the extent of the fouling region in order to make this prediction! Nevertheless, this is an interesting and unusual flow in that increasing the non-Newtonian nature of the fluid leads to an improved approximation.

Finally, we must note that the improvement in approximation is geometry-dependent. For a fracture that is anyway relatively long and thin, as $B \rightarrow \infty$ we may either (i) have no fouling at all or (ii) have a fouling layer that does not fill the entire wall profile at large B . Characteristics of the limit of large B relate to the limit of no flow along the fracture, which we study below in §4. Figure 8(c) illustrates the reduction in relative error, using (3.6) compared with (3.3), for two specific fracture geometries. We see that short-wavelength fractures are most affected by using (3.6).

4. The limit of no flow

We now address the limiting pressure gradient directly, which is known for many simple flows, e.g. in a pipe of diameter \hat{D} the pressure gradient must exceed $4\hat{\tau}_y/\hat{D}$ in order to flow. Critical pressure gradients are also known for many other duct cross-section shapes, following the seminal work of Mosolov & Miasnikov (1966, 1967), but these are 1D flows in uniform ducts of complex cross-section. Here, the flow is fully 2D, but physical intuition still suggests that a critical pressure drop is required in order to initiate flow.

One approach to finding the critical pressure drop would be to compute flows at successively larger pressure drops, until flow is initiated. However, the dimensionless

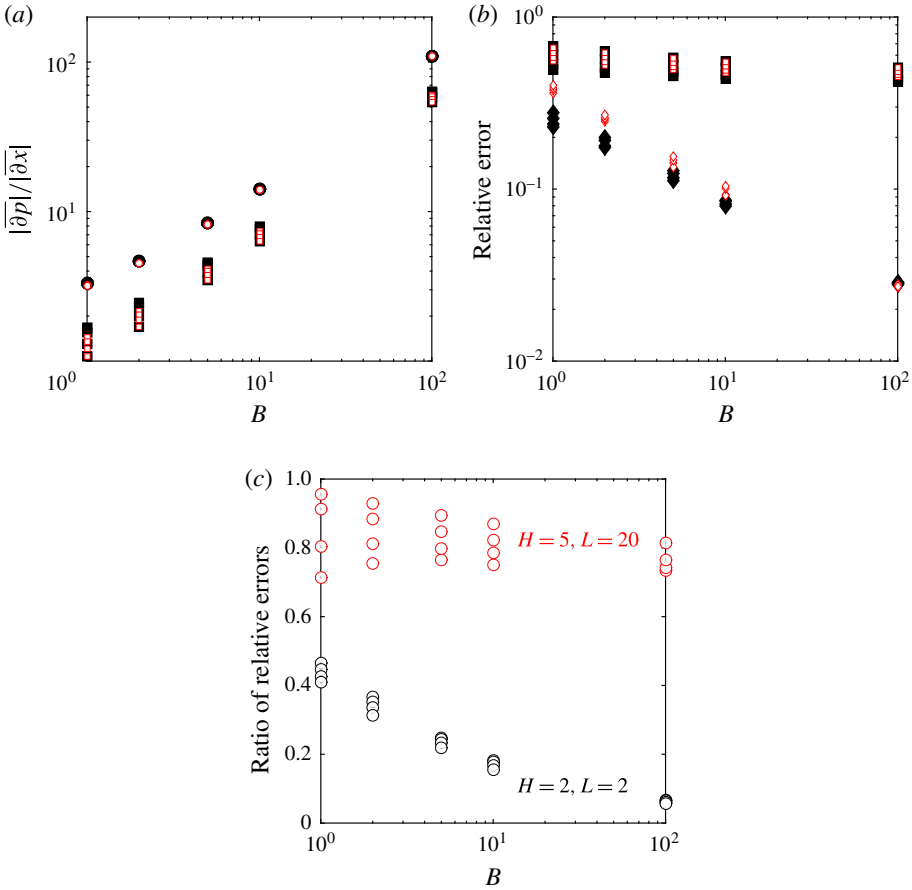


FIGURE 8. (Colour online) (a) Consistent errors in average pressure gradient prediction using (3.2), for $H=2, L=2$: black: wavy, red/white: triangular; circles: numerical, squares: lubrication approximation. (b) Relative error for the data in (a) (squares); relative error using the lubrication approximation (3.2) with the fracture width replaced by the yield surface position (diamonds). (c) Ratio of relative errors (lubrication approximation using yield stress position versus lubrication approximation using fracture width): $H=2, L=2$ in black; $H=5, L=20$ in red. It should be noted that the multiple points displayed at the same B correspond to different values of ψ .

formulation we have adopted appears to prevent this, since we have scaled with a mean velocity so that (2.9) is always satisfied. Thus, an alternative scaling is needed to study this limiting flow directly. Suppose therefore that we impose a fixed pressure drop $\Delta \hat{P}$ along the fracture. We then define a velocity scale \hat{U}^* to implicitly balance with the shear stress, i.e.

$$\frac{\Delta \hat{P}}{\hat{L}} = \frac{\hat{\mu} \hat{U}^*}{\hat{D}^2} \Rightarrow \hat{U}^* = \frac{\Delta \hat{P} \hat{D}^2}{\hat{L} \hat{\mu}}. \tag{4.1}$$

The viscous stresses and the modified pressure are scaled with $\hat{\mu} \hat{U}^* / \hat{D}$, the velocity is scaled with \hat{U}^* and lengths again with \hat{D} . This results in the same system (2.1)–(2.4b),

with all variables now designated with an asterisk to denote the different scaling. In place of B in the constitutive laws (2.4a) and (2.4b) we now have

$$Y \equiv \frac{\hat{\tau}_y \hat{D}}{\hat{\mu} \hat{U}^*} = \frac{\hat{L}}{\hat{D}} \frac{\hat{\tau}_y}{\Delta \hat{P}}, \tag{4.2}$$

representing the balance between the yield stress and the imposed pressure drop. We refer to Y as the yield number. The boundary conditions are again

$$\left. \begin{aligned} \mathbf{u}^* = 0, \quad & \text{at } y = 1 + y_+(x) \quad \text{and} \quad y = -1 - y_-(x), \\ \mathbf{u}^*(-L/2, y) &= \mathbf{u}^*(L/2, y), \\ \tau_{ij}^*(-L/2, y) &= \tau_{ij}^*(L/2, y), \\ p^*(-L/2, y) &= p^*(L/2, y) + L, \end{aligned} \right\} \tag{4.3}$$

i.e. now the pressure drop is known (with average gradient -1 along the fracture); the flow rate must be calculated. Our physical intuition about requiring a finite pressure drop to initiate flow along the fracture translates into the belief that there will be a critical value, say $Y = Y_c$, that separates flowing and static fractures. This notion will be made more precise below in §4.2.

As in either formulation described, the flow is a Stokes flow with a unique velocity solution, we expect that the solutions may be mapped to one another. Equivalence of the two formulations is established straightforwardly by rescaling, from which we deduce

$$Y = L \frac{B}{\Delta p} = Bq^*, \quad 2q^* = \int_{-1-y_-(x)}^{1+y_+(x)} u_1^*(x, y) dy, \tag{4.2a,b}$$

i.e. $2q^*$ is the areal flow rate from the imposed pressure formulation, which is equivalent to the inverse of the mean pressure gradient, $L/\Delta p$, computed in the imposed velocity formulation.

Although it is quite possible to compute \mathbf{u}^* from the imposed pressure formulation and then vary Y to study the limit of no flow, numerically this is less well conditioned than using the fixed flow rate formulation. Since the computational method is iterative and has tolerances imposed for convergence, it proves easier to impose a tolerance on an iteration for which $\mathbf{u} \sim O(1)$ than where $\mathbf{u}^* \rightarrow 0$. The identity (4.2) shows that it is feasible to work in this way. Using the imposed flow formulation, we find Δp as part of the solution and monitor convergence of $Y = LB/\Delta p \rightarrow Y_c$ as we increase B . We also see that if a critical stress balance is achieved, $\mathbf{u}^* \rightarrow 0$ (i.e. as $Y \rightarrow Y_c$), then implicitly $q^* \sim B^{-1}$ as $B \rightarrow \infty$.

4.1. Examples

We now examine three example sequences where we take increasingly large B at fixed geometry, to understand the limiting behaviour. For simplicity we fix $\psi = 0$. Figure 9 shows a relatively short fracture ($H = 1.5$, $L = 4$) at $B = 10, 100, 1000$. Even at $B = 10$, the majority of the flow is unyielded, with stationary fouling regions filling the deep parts of the fracture and an intact plug moving along the centre. These regions are separated by a thin shear layer that extends between the narrowest parts of the fracture, widening slightly at the deepest parts. As B increases, the width of this sheared layer is reduced, albeit slowly.

Next, we consider a relatively long fracture with small H/L ($H = 0.1$, $L = 20$); see figure 10. The flow has unyielded plug regions at the narrowest and widest parts of

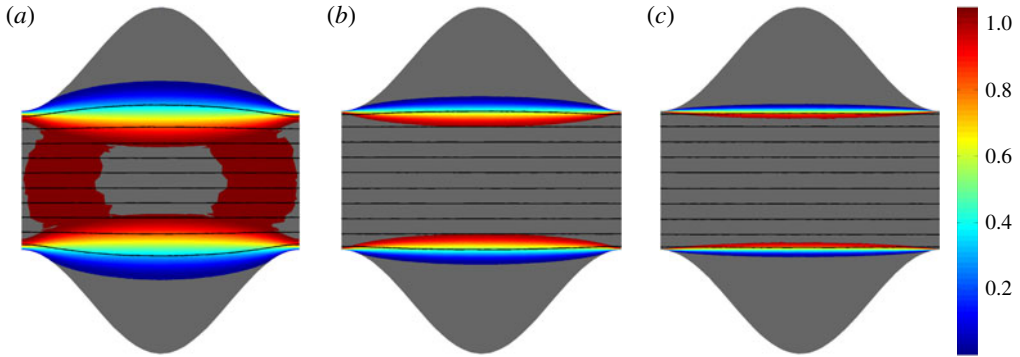


FIGURE 9. (Colour online) Colourmap of the speed with superimposed streamlines in a relatively short fracture $H = 1.5$, $L = 4$: increasing $B = 10, 100, 1000$ (from *a* to *c*). Unyielded regions are shown in grey.

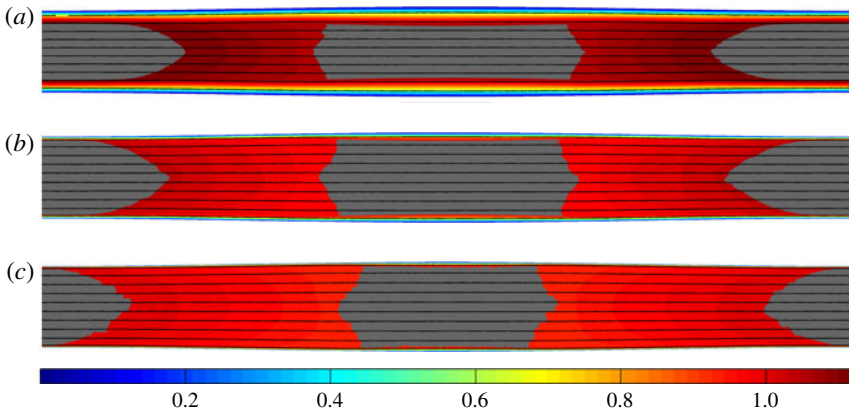


FIGURE 10. (Colour online) Colourmap of the speed with superimposed streamlines in a relatively short fracture $H = 0.1$, $L = 20$: increasing $B = 10, 100, 1000$ (from *a* to *c*). Unyielded regions are shown in grey.

the fracture, but no static fouling layers in the deepest parts of the fracture. The plug in the widest part is moving more slowly than that in the narrowest part, and these two plugs remain separated as B is increased.

Finally, we consider a more intermediate geometry ($H = 2, L = 20$); see figure 11. As may be expected, the limiting process at large B is qualitatively somewhere between the previous two examples. The narrowest and widest parts of the fracture have moving central plug regions, but there is also a static fouling layer in the deepest part of the fracture, extending between say $x \in (-x_f, x_f)$. The fouling layer and central plug are separated by a shear layer, which decreases slowly in width as B increases (similarly to the short fracture). The length x_f appears to approach a constant value as B increases. Similarly to the long fracture, the narrow and wide plugs remain separated at large B , moving at different speeds.

Figure 12 plots the variation of Y and $\Delta P/L$, with increasing B , for the three geometries illustrated in figures 9–11. We see that in all cases the computed Y appears to asymptote to a constant value at large B . This value denotes the critical

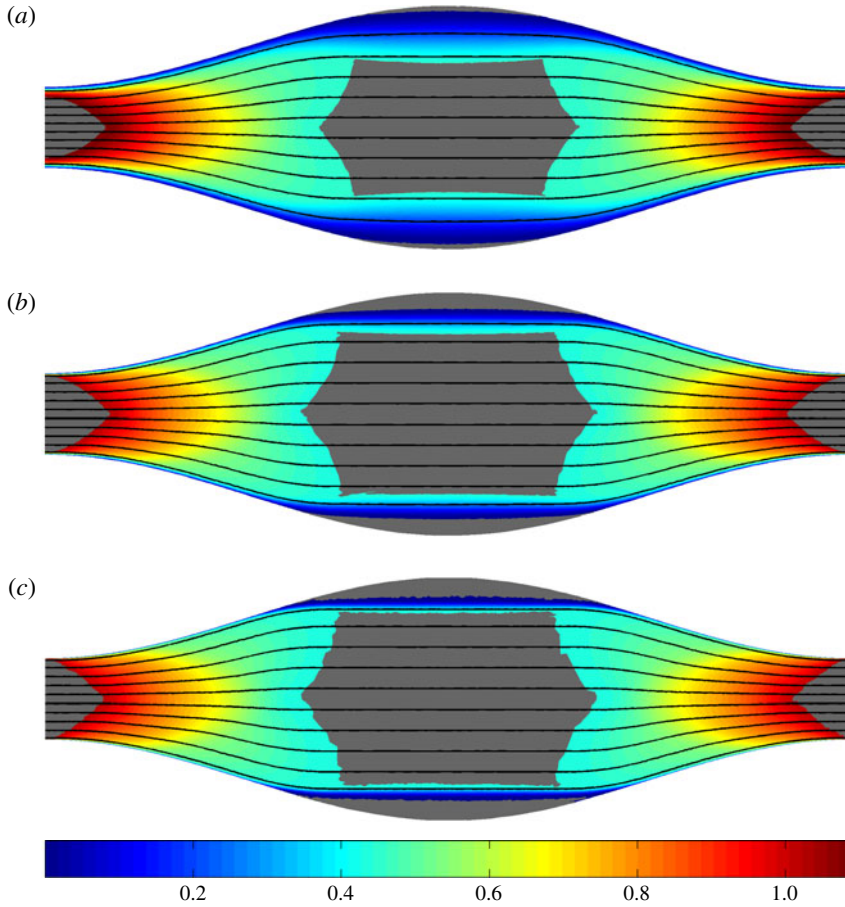


FIGURE 11. (Colour online) Colourmap of the speed with superimposed streamlines in a relatively short fracture $H = 2$, $L = 20$: increasing $B = 10, 100, 1000$ (from *a* to *c*). Unyielded regions are shown in grey.

limit Y_c . Interestingly, the short and long fractures appear to asymptote to $Y_c \approx 1$, whereas the intermediate geometry asymptotes to a value that is significantly larger. These examples are typical of the behaviour found over the whole range of our results.

4.2. The critical limit from a variational method

We now define the critical limit more precisely. Use of the imposed pressure formulation has some advantages for this, as we may use standard variational techniques (e.g. Putz & Frigaard 2010) to consider the zero flow limit. The solution \mathbf{u}^* satisfies

$$0 \leq a(\mathbf{u}^*, \mathbf{u}^*) = -Yj(\mathbf{u}^*) + L \int_{-1-y_-(x)}^{1+y_+(x)} u_1^*(x, y) dy \quad (4.5)$$

$$= -Yj(\mathbf{u}^*) + \int_{-L/2}^{L/2} \int_{-1-y_-(x)}^{1+y_+(x)} u_1^*(x, y) dy dx = Yj(\mathbf{u}^*) + Q(\mathbf{u}^*). \quad (4.6)$$

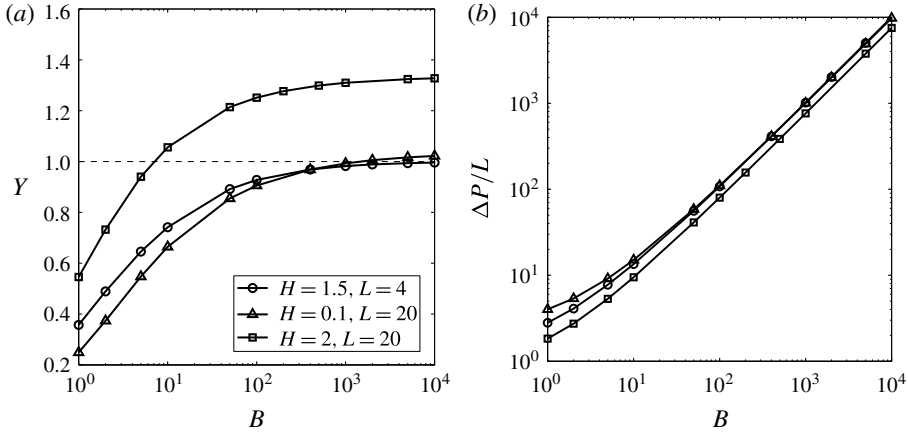


FIGURE 12. Limiting behaviour as $B \rightarrow \infty$ for the geometries of figures 9–11: (a) Y plotted against B ; (b) $\Delta P/L$ plotted against B .

The functionals $a(\mathbf{u}^*, \mathbf{u}^*)$ and $j(\mathbf{u}^*)$ denote respectively the viscous and plastic dissipation rate functionals:

$$a(\mathbf{u}^*, \mathbf{v}^*) \equiv \int_{-L/2}^{L/2} \int_{-1-y_-(x)}^{1+y_+(x)} \frac{1}{2} \dot{\gamma}_{ij}(\mathbf{u}^*) \dot{\gamma}_{ij}(\mathbf{v}^*) \, dy \, dx, \quad \mathbf{u}^*, \mathbf{v}^* \in \mathcal{V}, \tag{4.7}$$

$$j(\mathbf{v}^*) \equiv \int_{-L/2}^{L/2} \int_{-1-y_-(x)}^{1+y_+(x)} \dot{\gamma}(\mathbf{v}^*) \, dy \, dx, \quad \mathbf{v}^* \in \mathcal{V}. \tag{4.8}$$

It should be noted that we have extended the velocity integral at the inflow to the entire fracture:

$$Q(\mathbf{u}^*) \equiv \int_{-L/2}^{L/2} \int_{-1-y_-(x)}^{1+y_+(x)} u_1^*(x, y) \, dy \, dx, \tag{4.9}$$

as the flow rate is identical through each cross-section. Continuing this analysis,

$$0 \leq a(\mathbf{u}^*, \mathbf{u}^*) \leq -j(\mathbf{u}^*) \left[Y - \sup_{\mathbf{v}^* \in \mathcal{V}, \mathbf{v}^* \neq 0} \frac{Q(\mathbf{v}^*)}{j(\mathbf{v}^*)} \right] \equiv -j(\mathbf{u}^*) [Y - Y_c], \tag{4.10}$$

where \mathcal{V} denotes the space of admissible velocity solutions. The critical value of Y is thus formally defined as

$$Y_c = \sup_{\mathbf{v}^* \in \mathcal{V}, \mathbf{v}^* \neq 0} \frac{Q(\mathbf{v}^*)}{j(\mathbf{v}^*)}. \tag{4.11}$$

Following a similar procedure to Putz & Frigaard (2010) we can show that

$$a(\mathbf{u}^*, \mathbf{u}^*) \sim O([Y_c - Y]^2) \quad \text{as } Y \rightarrow Y_c^{*-}, \tag{4.12}$$

$$Yj(\mathbf{u}^*) \sim Q(\mathbf{u}^*) \sim O(Y_c - Y) \quad \text{as } Y \rightarrow Y_c^{*-}, \tag{4.13}$$

$$j(\mathbf{u}^*) \gtrsim \frac{a(\mathbf{u}^*, \mathbf{u}^*)}{[Y_c - Y]} \geq 0 \quad \text{as } Y \rightarrow Y_c^{*-}. \tag{4.14}$$

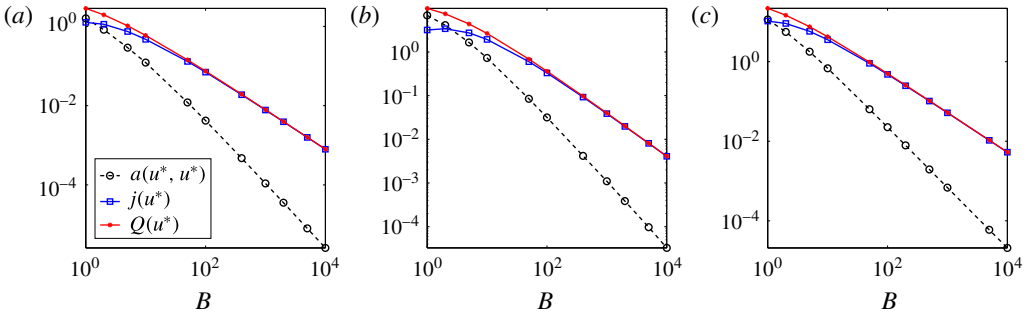


FIGURE 13. (Colour online) Viscous dissipation, plastic dissipation and flow rate, $a(u^*, u^*)$, $j(u^*)$ and $Q(u^*)$, for the three geometries illustrated in figures 9–11, from (a) to (c).

Figure 13 shows the computed values of $a(u^*, u^*)$, $j(u^*)$ and $Q(u^*)$ as B is increased, for the three geometries illustrated in figures 9–11. We see that $a(u^*, u^*)$ does indeed converge much faster than $j(u^*)$ and $Q(u^*)$, as is implicit in the above bounds. It should be noted that the $O([Y_c - Y]^2)$ in (4.12) is a lower bound on the decay rate of the viscous dissipation, and we can see that the decay rate is indeed faster than quadratic. Equation (4.14) ensures that the plastic dissipation decays to zero at least one order slower, and (4.13) ensures that the limiting balance is between the plastic dissipation and the flow rate. We again observe this in figure 13. This in turn can be used to argue that the supremum in (4.11) is in fact achieved by the solution. Indeed, if one knows the distribution of the limiting velocity solution, this can be used to estimate Y_c by inserting in (4.11). It should be noted that the size of the limiting velocity is not important in this determination as (4.11) is scale-invariant.

For computing the velocity, especially numerically, it can be more convenient to work with $O(1)$ quantities, e.g. in tracking convergence. In moving between formulations it is necessary to rescale velocities with q^* . Thus, to evaluate Y_c by inserting the limiting solution \mathbf{u}^* into (4.11), we may instead work directly with \mathbf{u} in the large B limit, i.e.

$$Y_c \sim \lim_{B \rightarrow \infty} \frac{Q(\mathbf{u})}{j(\mathbf{u})} = \lim_{B \rightarrow \infty} \frac{2L}{j(\mathbf{u})}, \tag{4.15}$$

on noting that $Q(\mathbf{u}) = 2L$ in the fixed flow rate formulation. In the next section we will estimate $j(\mathbf{u})$ in order to derive approximations to Y_c .

4.3. Characteristics of the different geometries

The flows illustrated in figures 9–11 represent the range of all observed behaviours (at least for $\Psi = 1$). By exploring these flows numerically as B is increased, we have been able to understand the different flow structures that emerge and in this way estimate the dominant contributions to $j(\mathbf{u})$ from each type of flow. This leads to a prediction of Y_c for the different fracture geometries. A summary of the results of this analysis follows, with the details confined to a number of appendices.

Short fractures. By short fractures we mean fractures in which we have observed a single central plug region along the fracture as $B \rightarrow \infty$, e.g. figure 9. The analysis of short fractures is presented in appendix A. We are able to deduce that these flows approach the same limit as that of a uniform channel, hence $Y_c = 1$. However, the

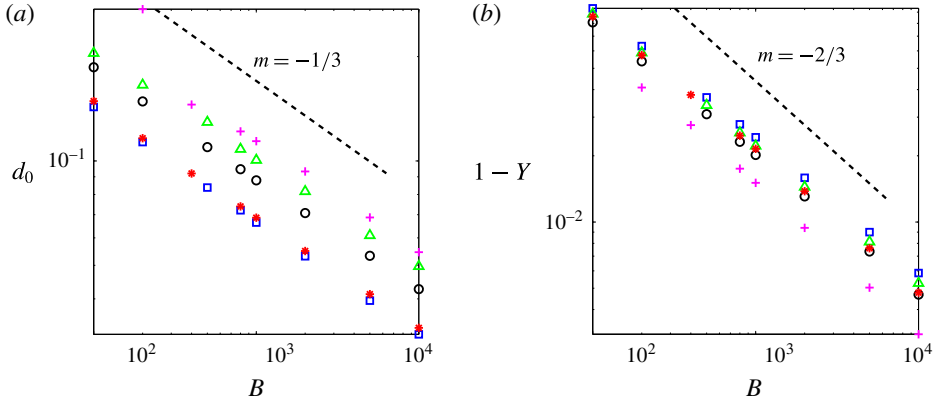


FIGURE 14. (Colour online) Limiting behaviour as $B \rightarrow \infty$ for five short fracture geometries: (a) shear layer thickness d_0 ; (b) $Y_c - Y$. Data are shown for (\circ , $H = 1, L = 3$), (\square , $H = 0.5, L = 2$), (\triangle , $H = 0.25, L = 4$), ($*$, $H = 3, L = 2$), ($+$, $H = 4, L = 4$); recall that $Y_c = 1$ for short fractures.

approach to the limit differs from that of a straight channel. As $B \rightarrow \infty$, $Y \rightarrow 1 - O(B^{-2k})$ and $d_0 \sim B^{-k}$ for some $k \in [1/3, 0.4]$. Here, d_0 represents the maximal width of the thin yielded shear layers observed. Figure 14 explores this convergence from our numerical results, taken from five different short fracture geometries, each as B is increased. It appears that, in fact, $d_0 \sim B^{-1/3}$ and $Y \rightarrow 1 - O(B^{-2/3})$, in accordance with this analysis. It should be noted that in a plane channel flow of a Bingham fluid, from the analytical solution as $B \rightarrow \infty$ we find $d_0 \sim B^{-1/2}$. Here, the yielded layer is different, being non-uniform and influenced by extensional stresses.

Long fractures with no fouling. The analysis of long fractures is presented in appendix B. We are able to deduce that

$$Y_c = \frac{1}{L} \int_{-L/2}^{L/2} \frac{1}{1+h} dx. \tag{4.16}$$

From the analysis we find $Y_c - Y \sim B^{-1/2}$ as $B \rightarrow \infty$, i.e. faster than convergence with B for the short fractures. Figure 15 illustrates the convergence rate of $Y_c - Y$ as $B \rightarrow \infty$ for one of our computed ‘long’ fractures. The $B^{-1/2}$ scaling is verified.

Intermediate fractures with partial fouling. We have seen that for both short and long fractures, it is possible to estimate the critical limit, essentially by using (3.2). For sufficiently short periodic fractures, the flow yields at the narrowest width, which means that (3.2) can be used, taking the modified fracture width from (3.6), which amounts to $h(x) \rightarrow 0$ as $B \rightarrow \infty$. For long enough fractures, no fouling occurs and (3.2) is applied directly. However, as we have seen in figure 11, for intermediate H/L , the limit $B \rightarrow \infty$ results in only a limited portion of the fracture being fouled, say $x \in [-x_f, x_f]$ for a symmetric fracture ($\psi = 0$). So far it is unclear (i) how to predict Y_c for such intermediate fractures, (ii) how the fouling length x_f is determined and (iii) what determines transitions from nominally short to intermediate to long fractures.

One feature observed in, e.g., figure 11 is that for intermediate H/L a significant portion of the fracture length remains yielded in the limit $B \rightarrow \infty$. Indeed, the limiting solutions appear to result in true unyielded regions only in the narrowest and widest parts of the fracture (approximately $x \in [-x_f, x_f]$), with a sheared pseudo-plug region

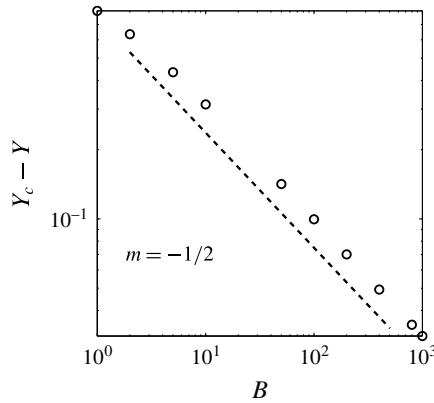


FIGURE 15. Convergence of $Y_c - Y$ ($Y_c = 1.227$) as $B \rightarrow \infty$ for $H = 1, L = 20$.

in between. The pseudo-plug region is of course necessary, since the true plug speeds in wide and narrow parts of the fracture are different. This type of pseudo-plug region arises in many viscoplastic flows

In appendix C, we first analyse the pseudo-plug, assuming that it is a lubrication flow limit (§ C.1), but discover that, in fact, the stress and velocity distributions are not compatible with this interpretation. This leads us to an empirical approach in which we fit a leading-order expression to the stress field (§ C.2). This understanding of the solution leads us, via an estimation of the plastic dissipation functional, to an approximation of Y as a function of the unknown x_f , as $B \rightarrow \infty$:

$$Y(x_f) \sim \frac{Q(\mathbf{u})}{j(\mathbf{u})} \approx \frac{L/2}{\int_{x_f}^{L/2} \frac{1}{1+h(x)} dx + \frac{x_f}{1+h(x_f)} + \pi \ln(1+h(x_f))} \tag{4.17}$$

(see § C.3). If we regard x_f as being selected by minimizing the strain rate, the actual x_f is determined by maximizing $Y(x_f)$ with respect to x_f , thus giving Y_c . It should be noted that the first two terms in the denominator of (4.17) effectively interpolate between the limiting Y_c derived for short channels ($x_f \rightarrow L/2$) and that for long channels with no fouling ($x_f \rightarrow 0$). The third term in (4.17) also vanishes as $x_f \rightarrow L/2$, so that the expression for short channels is contained in (4.17).

Figure 16(a) shows examples of the variation of $Y(x_f)$ computed from (4.17) for $L = 20, H = 0, 1, \dots, 8$ (black), and $L = 6, H = 0, 0.25, 0.5, \dots, 2$ (red). The maximum of $Y(x_f)$ is attained either at an endpoint or at the zero of

$$x_f = \pi(1+h(x_f)), \tag{4.18}$$

which is straightforwardly computed. For the examples shown, for $L = 6$ the maximum is $Y_c = 1$, attained at $x_f = L/2$, for all H . As $(1+h(x_f)) \in [1, 1+H]$, we see that the above equation has a root only for $L > 2\pi$. Since when this is not satisfied we find $Y_c = 1$, which is the short-fracture limit, we adopt the condition

$$L < 2\pi \tag{4.19}$$

as our definition of short fractures. At larger L we see that there is a maximum in $(0, L/2)$ and compute this numerically. As $L \rightarrow \infty$ we find that $2x_f/L \rightarrow 0$ since

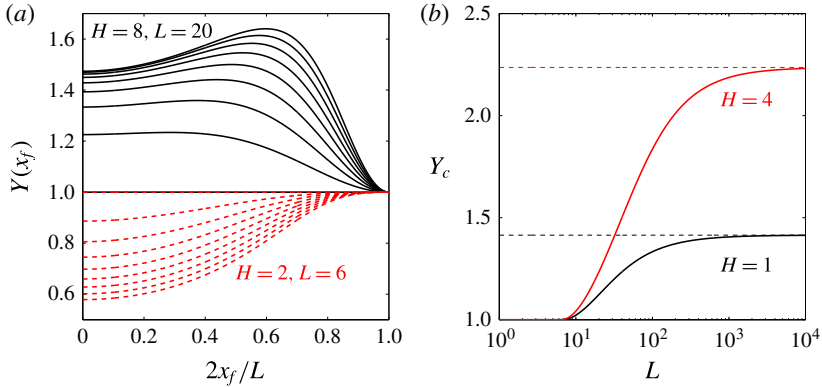


FIGURE 16. (Colour online) (a) Variation of $Y(x_f)$ from (4.17) for $L=20, H=0, 1, \dots, 8$ (black); $L=6, H=0, 0.25, 0.5, \dots, 2$ (red). (b) Variation of Y_c (computed by maximizing $Y(x_f)$ in (4.17)) with L for $H=1$ (black) and $H=4$ (red). Broken lines indicate the limit of Y_c with no fouling.

$x_f \rightarrow (1 + H)\pi$. The second and third terms in the denominator of (4.17) then become $O(1/L)$ smaller than the first one, which converges to Y_c for the long-fracture limit without fouling. Figure 16(b) shows the variation of Y_c with L for two values of H , computed as the maximum of (4.17). For L satisfying (4.19) we see that $Y_c = 1$, increasing smoothly to the asymptotic values for no fouling at large L , marked with the broken lines.

We have computed Y_c from this toy model, by maximizing (4.17) over x_f , and compare this with the values of Y_c from our 2D computations. The agreement is reasonable, as is shown in figure 23 in § C.3. Although reasonable, it is possible to improve (4.17) by a better estimate of $j(\mathbf{u})$ in which the pseudo-plug stresses use a more accurate approximation. This derivation is detailed in § C.4, resulting in

$$Y(x_f) \sim \frac{Q(\mathbf{u})}{j(\mathbf{u})} \approx \frac{L/2}{\int_{x_f}^{L/2} \frac{1}{1+h(x)} dx + \frac{x_f}{1+h(x_f)} + \pi \int_{x_f}^{L/2} \frac{|h'|}{(1+h)} \frac{1}{1+\sqrt{f_0|h'|}} dx}, \quad (4.20)$$

where f_0 is a constant (see § C.4). We again find x_f by maximizing Y_{x_f} . This results in Y_c and x_f as illustrated in figure 17(a,b) respectively. We observe a general increase in Y_c and a small shift in x_f compared with (4.17). The relative error with the computed 2D results is however diminished, see figure 17(c), now typically remaining below 10% for most of the parameter space.

4.4. Affine fractures

Finally, we present some examples of the limiting process in affine fractures. Three different styles of affine fracture are generated for intermediate $H=2, L=20$. Figure 5 earlier and figures 18 and 19 below present the sequence $B=100, 1000, 10000$ for each fracture, plotting the speed, streamlines and unyielded plug regions. In general, we observe that the small-scale fracture roughness is always fouled. As B increases, a larger fraction of the fracture becomes immobilized. The boundaries of the flowing

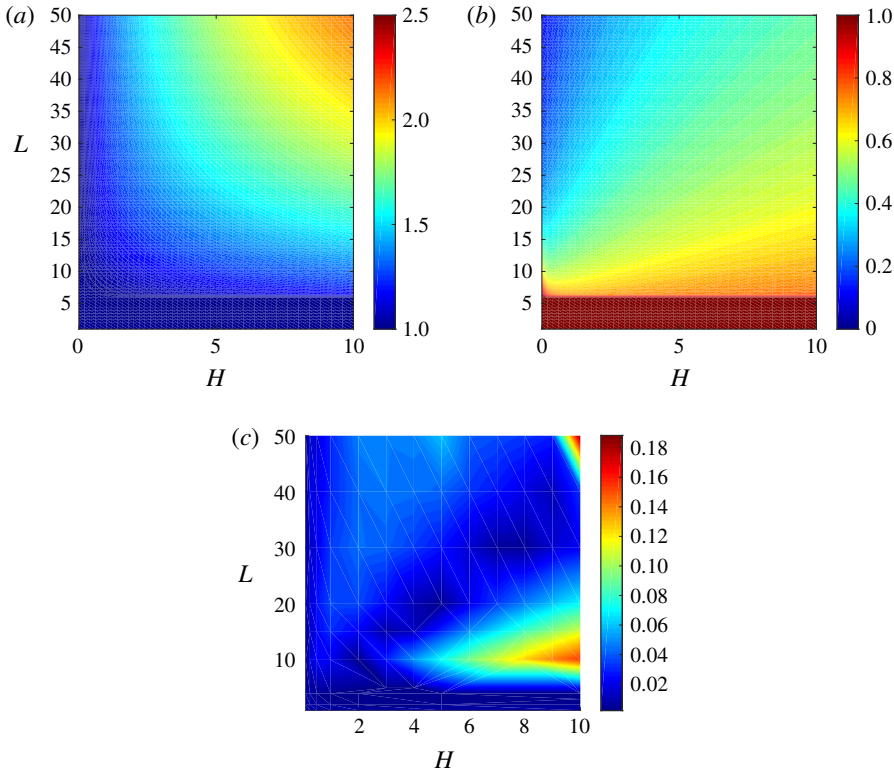


FIGURE 17. (Colour online) (a) Variation of Y_c computed by maximizing (4.20). (b) Variation of the value of x_f that maximizes (4.20), scaled with $L/2$. (c) Absolute relative error between (a) and our Y_c calculated from the 2D computations.

part of the fracture are formed by arc-like surfaces that span between locally narrow points of the fracture wall. The radius of curvature of these surfaces increases with B .

It is notable that as B increases, the self-selected flowing channel geometry consists of a series of joined segments along which the streamlines are approximately parallel. In such sections, shear components evidently dominate. These parallel segments are connected by angular converging and diverging segments, in which extensional stresses and strain rates will be significant. The limiting process as $B \rightarrow \infty$ appears to result again in a combination of thin yielded shear layers and non-vanishing $O(1)$ pseudo-plug regions. Although the evident complexity of the self-selection and limiting processes so far eludes a simple explanation, there is some hope that these component structures can be understood. Thus, if one can first understand the geometric features of flow self-selection (meaning the fouling process and orientation of the flowing part of the fracture, generating tortuosity) it should be possible to estimate the critical pressure drops (or yield stresses).

More quantitatively, we may evaluate Y_c for these geometries from the computed 2D solution. Figure 20 shows convergence of $Y \rightarrow Y_c$ as $B \rightarrow \infty$. The symmetric fracture has the smallest Y_c , and also appears to have the more constricted flow apertures. The other two geometries appear to compensate increasing tortuosity (smaller Y) with a larger effective channel width (larger Y).

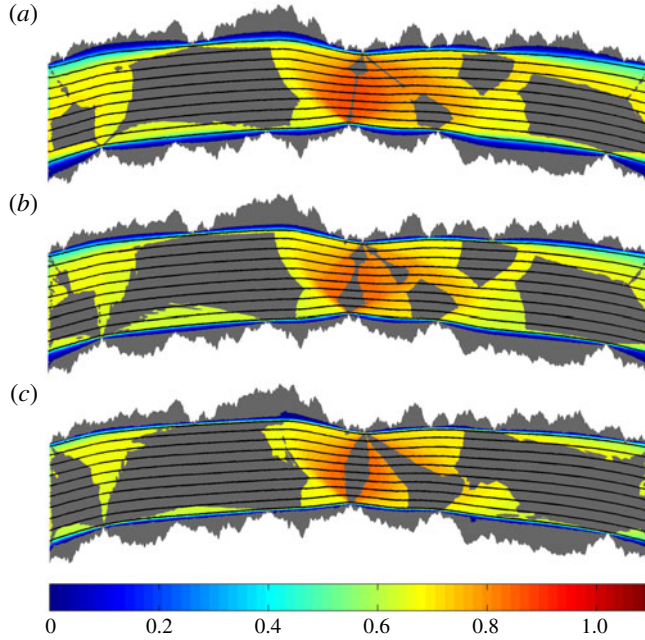


FIGURE 18. (Colour online) Computed examples of speed $|\mathbf{u}|$ and streamlines for a fracture formed from two different affine surfaces. The parameters are $H = 2$, $L = 20$, $B = 100, 1000, 10000$, from (a) to (c), with (grey) unyielded plugs.

5. Discussion/conclusions

In this study we have investigated the two-dimensional flow of a Bingham fluid along an uneven fracture. The work has two principal foci. The first is to determine numerically the flow-rate–pressure-drop relationship in such geometries (the appropriate Darcy law), to understand better the limits of simple approximations that are presently used in a somewhat *ad hoc* manner. Second, we explore the limiting values of the pressure drop (equivalently yield stress) at which non-zero flows are first found. This question has critical consequences for the study of flow onset in pressure-driven porous media flows, i.e. selection of the critical initial path, as well as helping to provide practical estimates for invasive sealing of porous media/channels, i.e. how far will a sealing fluid penetrate under a given driving pressure?

The initial part of the paper has extensively studied geometric effects in idealized fractures (periodic with wavy or triangular profiles) of dimension (H, L) . Strict application of lubrication/Hele-Shaw approximations to the flow to provide (nonlinear) Darcy-type flow laws has been shown to be limited to $H/L \ll 1$, as may be expected. As a rule of thumb, errors of 10% or less appear to require $H/L \lesssim 1/20$. For geometries outside these limits, flow approximations are vulnerable to similar effects to Newtonian fluids, e.g. development of tortuosity, etc. One significant difference between Newtonian and Bingham (or other generalized Newtonian) fluids is in the coupling of geometrical and rheological parameters in the flow law. In the Newtonian fluid literature, there are many efforts to improve and extend Darcy-law-type estimates to these situations. Here, we have resisted the temptation to develop analogous methods. It is clear that some of these methods would be effective, especially in the

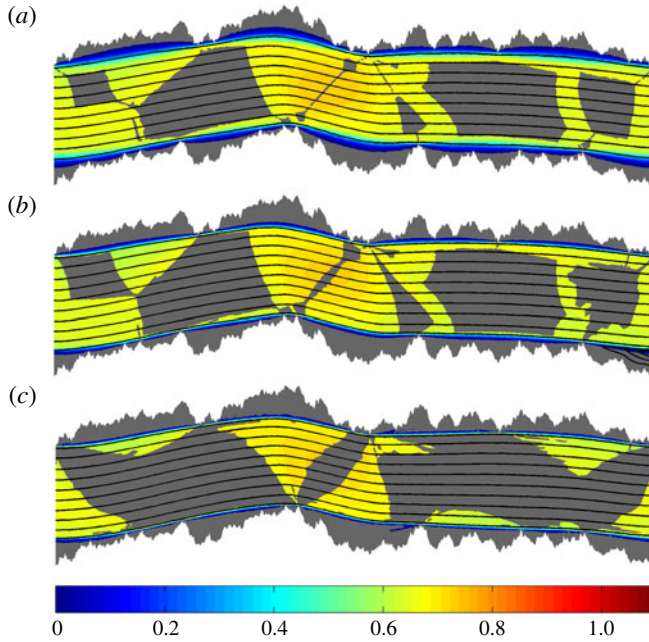


FIGURE 19. (Colour online) Computed examples of speed $|u|$ and streamlines for a fracture formed from two identical affine surfaces, shifted. The parameters are $H = 2$, $L = 20$, $B = 100, 1000, 10000$, from (a) to (c), with (grey) unyielded plugs.

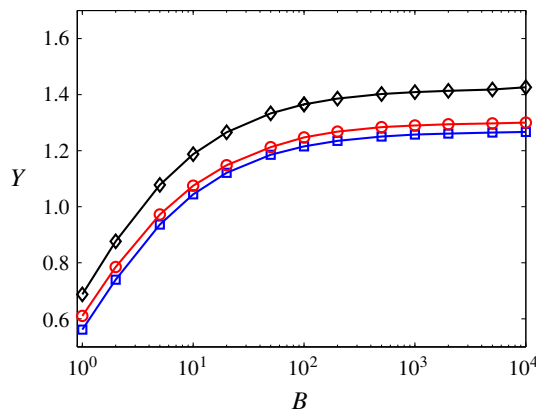


FIGURE 20. (Colour online) Computed yield number as a function of the Bingham number for the three different affine fractures of figures 5–19. Blue squares: the two surface are symmetrical. Red circles: the two surfaces are uncorrelated. Black lozenges: the two surfaces are identical, shifted laterally with a constant gap.

limit of low B and for H/L increasing away from the lubrication limit, but inflection of this algebraic misery on the reader is left to other researchers.

Moving to larger B or for $H/L \ll 1$, a more serious limitation of lubrication-type approximations to the Darcy law emerges. Unyielded fluid appears at the wall in deeper parts of the fracture (fouling layers). Fouling layers provide an $O(1)$ adjustment

of the flowing area and hence $O(1)$ errors in the predictions of lubrication-type approximations. We have demonstrated that these errors can be reduced significantly by adopting the yield surface of the fouling layers as the new fracture wall and applying the usual lubrication approximation. Therefore, approximation of the flow law presents no particular problem provided that the fouling layers are known. Unfortunately, this is not the case as the fluid self-selects the flowing area.

Previous work has addressed the question of the onset of fouling in idealized geometries with $O(1)$ variations (Roustaei & Frigaard 2013; Roustaei *et al.* 2015). Smaller-scale roughness also seems to readily foul, although to the best of our knowledge this has not been quantified. At intermediate B , estimation of the degree of fouling appears to be difficult, as a general problem for which one would like to specify a simple predictive closure relationship. However, numerical solution as here is an effective tool even for the very complex affine geometries, and can be easily extended to more general yield stress fluid models. Although Newtonian fluids do not foul and self-select, sufficiently deep undulations do result in zones of recirculation. This link is explored in Roustaei & Frigaard (2013). Thus, except for very large B , it may be that the range of speeds encountered in Bingham and Newtonian fluids flowing through the same geometry may not differ significantly. This is also observed in packed-bed models of porous media at fixed flow rates (Chevalier *et al.* 2013a; Bleyer & Coussot 2014).

A significant part of the paper has considered the limit of no flow, $B \rightarrow \infty$, which via a rescaling can be characterized with the yield number:

$$Y \equiv \frac{\hat{L} \hat{\tau}_Y}{\hat{D} \Delta \hat{P}}, \quad (5.1)$$

directly representing the balance between the applied pressure and the resisting yield stress. Above a critical value Y_c there is no flow. On the theoretical side, we have formally characterized Y_c as a limiting ratio of flow rate to plastic dissipation, shown that this limit is attained by the velocity solution and provided general bounds on convergence of the viscous dissipation, plastic dissipation and flow rate in the limit $Y \rightarrow Y_c^-$. We have then studied the approach to Y_c numerically and asymptotically for simpler symmetric fracture geometries, deriving the leading-order behaviour in the cases of both short and long-thin fractures.

For short fractures, we find that $Y_c = 1$: at large B the flow consists of an intact central plug region separated from the walls (and fouling layers) by a progressively thinning shear layer. This limit is analogous to the flow in a uniform channel, for which also $Y_c = 1$. Short fractures, for the purposes of this limiting process, are defined as $L < 2\pi$. For long-thin fractures, no fouling occurs and the lubrication approximation is valid. The critical yield number can be approximated from the harmonic mean of the fracture width. However, application of this naive approximation more widely will incur $O(1)$ errors, and we have seen that the lubrication approximation is quite limited.

Intermediate fractures are more interesting. The central plug region here is broken into two parts (in wide and narrow parts of the fracture) and remains so as $B \rightarrow \infty$. The plug in the widest part occupies a length approximately equal to that of the fouling layer (defined as $2x_f$), whereas the size of plugs in the narrowest part of the fracture remains of $O(1)$. Between the two plug regions, we find a slightly sheared pseudo-plug region. The pseudo-plug joins to the wall in a narrow layer of high shear, and a similar high-shear layer separates fouling layers and the central plug in the wide part of the fracture. Based on these observations, we have proposed a rather simple

toy model to describe the limiting flows. In each of the above regions, we are able to estimate the strain rate and hence construct an approximation to the plastic dissipation that depends only on the single parameter x_f , the half-length of the fouled layers. By minimizing the plastic dissipation at fixed flow rate we are able both to estimate x_f and to calculate the limiting Y_c . The relative errors in this crude approximation are typically $\lesssim 10\text{--}15\%$, allowing us to effectively predict the critical pressure for the onset of flow.

We have also performed several simulations in self-affine fractures, as shown in figures 5–19. Although these geometries deserve a far more complete study, we may infer some trends from our current results. First, both pseudo-plugs and fouling layers are present in affine fractures. Second, the limiting zero flow behaviour again appears to be characterized by geometries that simplistically are componentwise constructed of shear layers, pseudo-plugs and fouled regions. This leads us to the conclusion that to understand the flow one needs to understand how the fouling layer is self-selected. It seems, for instance, obvious that it acts as a filter for the small scales – the roughness problem. It is, however, unclear how the larger-scale heterogeneities are filtered. Similarly to the wavy fractures, the final selected flowing channel seems to have a rather constant width, at least in sections.

Finally, we may consider to what extent our results are valid for more complex viscoplastic fluids, e.g. Herschel–Bulkley fluids. First, the type of Hele-Shaw/lubrication approach is straightforwardly derived and the numerical code may be extended to such fluids with little additional effort. We expect a very similar set of limits (in terms of $H/L \ll 1$) for application of the lubrication approximations. At intermediate B , H and L , we expect to see different solutions according to the different constitutive laws, but qualitatively similar to those reported earlier.

Insofar as determining the critical Y goes, the situation is only partly clear. First, from the theoretical perspective, the definition of Y_c is analogous (except that the test space for solutions may be different – depending on the power-law index n). It is slightly more complex to show that the viscous dissipation converges faster than the plastic dissipation as $Y \rightarrow Y_c$, but this is also the case. Since the critical limit has no deformation, i.e. the flow has stopped, it simply represents an admissible stress solution to the Stokes equations. This means that Y_c will be the same for all yield stress fluids satisfying the von Mises yield criterion. This fact could be established more formally by using the stress maximization principle. As a consequence, we would also expect a qualitatively similar structure to the flow at large B . However, the actual limiting behaviour as $B \rightarrow \infty$ may differ with n , e.g. convergence rate of d_0 .

Acknowledgements

Part of this research has been carried out at the University of British Columbia, supported financially by NSERC and Schlumberger through CRD project 444985-12. A research visit to FAST was funded by the Université Paris-Sud and the ANR programme LaboCothep ANR-12-MONU-0011.

Appendix A. Short fractures: qualitative analysis

In short fractures, we have seen that increasingly narrow sheared layers separate fouling layers and the moving plug. As the plug remains intact as $B \rightarrow \infty$, from mass conservation we may assume that the plug velocity $u_p \sim 1$. There is an evident symmetry in the shape of the sheared regions, which we assume can be reasonably approximated by boundaries, $y = \pm[y_c \pm d_0(B, x)]$, in the upper and lower sheared

layers respectively. Here, $y = \pm y_c$ denote the central positions of the sheared layers at $x = 0$. To leading order we may expect that within the sheared layers

$$\dot{\gamma}(\mathbf{u}) \sim \left| \frac{\partial u}{\partial y} \right| \sim O\left(\frac{u_p}{d_0}\right). \tag{A 1}$$

On integrating first with respect to y and then along the sheared layer, we find a leading-order contribution to $j(\mathbf{u})$, of size $\sim u_p L$, from each sheared layer. Therefore, we find that $j(\mathbf{u}) \sim 2u_p L \sim 2L$, and hence that $Y_c \sim 1$, as observed.

We may extend this analysis to examine the convergence of $Y \rightarrow Y_c^-$. Let us suppose that $d_0(B, 0) \sim B^{-k}$ as $B \rightarrow \infty$. Examination of the velocity profile at $x = 0$ reveals that $u(0, y)$ shows a variation across the sheared layer that is approximately cubic in $y \mp y_c$. This leads to the approximation

$$u(x, y) \approx \frac{u_p}{2} - \frac{3u_p}{2} \left[\left(\frac{y - y_c}{d_0(B, x)} \right) - \frac{1}{3} \left(\frac{y - y_c}{d_0(B, x)} \right)^3 \right] \tag{A 2}$$

in the upper sheared layer. In fact, as the ends $x = \pm L/2$ are approached, the cubic approximation changes to quadratic, but at the same time $d_0(B, x)$ decreases, so that contributions from these regions are smaller. It can be observed that the above profile integrates in y to satisfy the flow rate constraint exactly with $u_p = 1$ (and analogously in the lower shear layer). The leading-order components of the shear rate are

$$\dot{\gamma}_{xy} \sim \frac{\partial u}{\partial y} \approx -\frac{3}{2d_0} \left[1 - \left(\frac{y - y_c}{d_0} \right)^2 \right], \quad \dot{\gamma}_{xx} \sim 2 \frac{\partial u}{\partial x} \approx 3 \frac{d'_0}{d_0} \left[\left(\frac{y - y_c}{d_0} \right) - \left(\frac{y - y_c}{d_0} \right)^3 \right]. \tag{A 3a,b}$$

As the sheared layers are relatively long and thin, we may assume that $|d'_0(B, x)| \sim d'_0(B, 0)/L \ll 1$, and therefore find in the upper layer

$$\begin{aligned} \dot{\gamma}(\mathbf{u}) &\approx \frac{3}{2d_0} \left[1 - \left(\frac{y - y_c}{d_0} \right)^2 \right] \left[1 + 4[d'_0]^2 \frac{\left[\left(\frac{y - y_c}{d_0} \right) - \left(\frac{y - y_c}{d_0} \right)^3 \right]^2}{\left[1 - \left(\frac{y - y_c}{d_0} \right)^2 \right]^2} \right]^{1/2} \\ &\sim \frac{3}{2d_0} \left[1 - \left(\frac{y - y_c}{d_0} \right)^2 \right] + \frac{3[d'_0]^2}{d_0} \left[\left(\frac{y - y_c}{d_0} \right)^2 - \left(\frac{y - y_c}{d_0} \right)^4 \right] + O([d'_0]^4), \end{aligned} \tag{A 4}$$

and a similar contribution from the lower layer. Integration over the two sheared layers gives

$$j(\mathbf{u}) \sim 2L + \frac{8}{5} \int_{-L/2}^{L/2} [d'_0]^2 dx, \tag{A 5}$$

and therefore, as $B \rightarrow \infty$,

$$Y \sim \frac{Q(\mathbf{u}^*)}{j(\mathbf{u}^*)} = \frac{Q(\mathbf{u})}{j(\mathbf{u})} \sim 1 - \frac{4}{5L} \int_{-L/2}^{L/2} [d'_0]^2 dx \sim 1 - O\left(\frac{1}{L^2 B^{2k}}\right). \tag{A 6}$$

Therefore, we have $Y_c - Y \sim L^{-2}B^{-2k}$, and since also $Y = Bq^*$, as $B \rightarrow \infty$ we have $q^* \sim 1/B - O(L^{-2}B^{-2k-1})$. Returning now to (4.13),

$$Q(\mathbf{u}^*) = 2Lq^* \sim 2L/B - O(L^{-1}B^{-2k-1}) \sim O(Y_c - Y) \sim O(L^{-2}B^{-2k}). \tag{A 7}$$

This implies that $k \leq 1/2$ is the maximal convergence rate for the width of the sheared layer in short fractures (recall that $d_0(B, 0) \sim B^{-k}$).

Following similar lines, for short fractures, we may deduce that $a(\mathbf{u}^*, \mathbf{u}^*) \sim L(q^*)^2/d_0$ as $B \rightarrow \infty$. From the bound (4.12), we deduce that

$$LB^{-2+k} \sim L(q^*)^2/d_0 \sim a(\mathbf{u}^*, \mathbf{u}^*) \sim O([Y_c - Y]^2) \sim O(L^{-4}B^{-4k}), \implies 5k \leq 2, \tag{A 8}$$

i.e. $k \leq 0.4$. Finally, we examine (4.14):

$$LB^{-1} \sim Lq^* \sim j(\mathbf{u}^*) \gtrsim \frac{a(\mathbf{u}^*, \mathbf{u}^*)}{[Y_c - Y]} \sim \frac{L(q^*)^2}{d_0L^{-2}B^{-2k}} \sim L^3B^{3k-2} \implies k \geq 1/3. \tag{A 9}$$

Appendix B. Long fractures: qualitative analysis

In a long symmetric fracture, we commonly observe true plug regions in the widest and narrowest parts of the fracture, separated by pseudo-plug regions. For $L \gg 1$, we can expect that the flow is pseudo-1D and that the lubrication approximation should give a reasonable estimate of the pressure gradients and flow velocity. Indeed, this has been verified in § 3. Therefore, we may use the lubrication pressure gradient to evaluate the limiting Y . At large B , we may expand (3.1) in series form:

$$\phi \sim 1 - \frac{\sqrt{2}}{(1+h)B^{1/2}} + \frac{2}{3(1+h)^2B} + \frac{\sqrt{2}}{9(1+h)^3B^{3/2}} + \dots \tag{B 1}$$

Thus, the total pressure drop is

$$\Delta p = \int_{-L/2}^{L/2} \left| \frac{\partial p}{\partial x} \right| dx = \int_{-L/2}^{L/2} \frac{B}{(1+h)\phi} dx, \tag{B 2}$$

$$\sim B \int_{-L/2}^{L/2} \frac{1}{1+h} + \frac{\sqrt{2}}{(1+h)^2B^{1/2}} + O(B^{-1}) dx, \tag{B 3}$$

$$Y = \frac{BL}{\Delta p} \sim \frac{L}{\int_{-L/2}^{L/2} \frac{1}{1+h} dx + \frac{\sqrt{2}}{B^{1/2}} \int_{-L/2}^{L/2} \frac{1}{(1+h)^2} dx + O(LB^{-1})}, \tag{B 4}$$

$$\sim \left(\frac{1}{L} \int_{-L/2}^{L/2} \frac{1}{1+h} dx \right)^{-1} \left[1 - \frac{\sqrt{2}}{B^{1/2}} \frac{\frac{1}{L} \int_{-L/2}^{L/2} \frac{1}{(1+h)^2} dx}{\frac{1}{L} \int_{-L/2}^{L/2} \frac{1}{1+h} dx} + O(B^{-1}) \right]. \tag{B 5}$$

The first term above is clearly Y_c , and can be derived by effectively integrating the yield stress along the slowly varying wall. For example, for the wavy interface we find the expression

$$Y_c = \sqrt{1 + H + \frac{1 - \cos(\pi\psi)}{8} H^2}. \tag{B 6}$$

Referring back to figure 10 and the limiting behaviour illustrated in figure 12, we note that typically $Y_c > 1$ for this flow regime. The condition for having no fouling layer seems to require a small ratio H/L . Provided that this is satisfied, Y_c is in fact independent of L . In the example shown, since we have small H it appears that $Y_c \approx 1$, but this need not be the case.

From the analysis leading to (B 5), we see that $Y_c - Y \sim B^{-1/2}$ as $B \rightarrow \infty$, i.e. faster than convergence with B for the short fractures. Comparing with the bounds (4.12)–(4.14) we deduce that

$$q^* \sim \left(\frac{B}{L} \int_{-L/2}^{L/2} \frac{1}{1+h} dx \right)^{-1} + O(B^{-3/2}), \quad j(\mathbf{u}^*) \sim \frac{2L}{B} + O(B^{-3/2}), \quad \text{as } B \rightarrow \infty, \tag{B 7a,b}$$

and the following bound:

$$a(\mathbf{u}^*, \mathbf{u}^*) \lesssim O(B^{-3/2}), \quad \text{as } B \rightarrow \infty. \tag{B 8}$$

Appendix C. Intermediate fractures: qualitative analysis

Figure 11 shows that for intermediate H/L , a significant portion of the fracture length remains yielded in the limit $B \rightarrow \infty$. Indeed, the limiting solutions appear to result in true unyielded regions only in the narrowest and widest parts of the fracture (approximately $x \in [-x_f, x_f]$), with a sheared pseudo-plug region in between. The pseudo-plug region is of course necessary, since the true plug speeds in wide and narrow parts of the fracture are different. This type of pseudo-plug region arises in many viscoplastic flows.

We first analyse the pseudo-plug, assuming that it is a lubrication flow limit (§ C.1). We discover that, in fact, the stress and velocity distributions are not compatible with this interpretation. This leads us to an empirical approach in which we fit a leading-order expression to the stress field (§ C.2). This appreciation of the solution leads to an approximation of Y , as a function of the unknown x_f , which is maximized to find both x_f and Y_c . We first introduce this for a simple qualitative approximation of the plastic dissipation in § C.3 and then improve the estimate in § C.4.

C.1. The classical pseudo-plug procedure

Analysis of the pseudo-plug region stems from the studies of Walton & Bittleston (1991) and Balmforth & Craster (1999). We examine this approach as offering a potential description of the pseudo-plug observed here. In this approach, the plug velocity is derived from the Buckingham–Reiner equation (3.1), which is approximated at large B by (B 1). From ϕ we deduce the yield surface position at $y = \pm y_Y(x) = (1 + h(x))\phi$:

$$y_Y(x) \sim 1 + h(x) - \frac{\sqrt{2}}{B^{1/2}} + \frac{2}{3(1+h(x))B} + \frac{\sqrt{2}}{9(1+h(x))^2 B^{3/2}} + \dots \tag{C 1}$$

Interestingly, the thickness of the high-shear layer is independent of $h(x)$ to leading order at large B , simply following the wall profile. The pseudo-plug velocity to leading order is calculated as

$$u_{p,0} \sim \frac{1}{1+h} \left[1 + \frac{\sqrt{2}}{3(1+h)B^{1/2}} - \frac{16}{9(1+h)^2 B} + O((1+h)^{-3} B^{-3/2}) \right]. \tag{C 2}$$

As for the thin shear layers observed in short fractures, we deduce that $\dot{\gamma}_{xy} \sim u_{p,0} B^{1/2}$ within the sheared layer. The size of $\dot{\gamma}_{xx}$ comes from differentiating $u_{p,0}$ with respect to x , i.e.

$$|\dot{\gamma}_{xx}| \sim \left| \frac{dh}{dx} \right| \sim \frac{1}{L}, \tag{C3}$$

since the x -dependence is through both $h(x)$ and $y_Y(x)$, both derivatives of which scale with dh/dx at large B (we assume $H \sim O(1)$).

In the sheared layers, the leading-order shear rate varies linearly with y :

$$\frac{\partial u}{\partial y} \sim \dot{\gamma}_{xy} = \dot{\tau}_{xy} + B \sim B \left(1 - \frac{y}{y_Y} \right), \tag{C4}$$

so that the velocity profile is parabolic in y . It becomes apparent that the scaling arguments that have been made (i.e. assuming $|\dot{\gamma}_{xy}| \gg |\dot{\gamma}_{xx}|$) break down as $y \rightarrow y_Y^+$ and more specifically for

$$y - y_Y \sim \frac{dh}{dx} B^{-1} \sim \frac{1}{BL}. \tag{C5}$$

The above is the usual argument for emergence of a pseudo-plug region, within which the strain rates are of comparable size. Since within any pseudo-plug the main cause of straining will come from the geometrical changes, we may assume that $|\dot{\gamma}_{xy}| \sim |\dot{\gamma}_{xx}| \sim |dh/dx| \sim 1/L$. Therefore, within the pseudo-plug we expect that

$$\tau_{ij} = \left[1 + \frac{B}{\dot{\gamma}} \right] \dot{\gamma}_{ij} \sim B \frac{\dot{\gamma}_{ij}}{\dot{\gamma}} \left[1 + O\left(\frac{1}{BL} \right) \right]. \tag{C6}$$

At leading order, therefore, we have that $\tau = B$ in the pseudo-plug.

For large L , the x -momentum equation at leading order in the pseudo-plug still does not include τ_{xx} . It follows that

$$\tau_{xy} \sim -B \frac{y}{1+h(x)}, \quad \tau_{xx} \sim -\text{sign}(h'(x)) B \sqrt{1 - \frac{y^2}{(1+h(x))^2}}, \tag{C7a,b}$$

noting that $y_Y(x) \sim 1+h(x)$. Equally, we may deduce that to leading order

$$\dot{\gamma}_{xx} \sim -\frac{2h'(x)}{(1+h(x))^2}, \quad \dot{\gamma}_{xy} \sim \frac{-y|\dot{\gamma}_{xx}|}{\sqrt{y^2 + (1+h(x))^2}}, \tag{C8a,b}$$

which may be integrated to give the velocity distribution across the pseudo-plug:

$$u \sim u_{p,0} + |\dot{\gamma}_{xx}| \left[\sqrt{2}(1+h(x)) - \sqrt{y^2 + (1+h(x))^2} \right]. \tag{C9}$$

It should be noted that under the assumption of near-parallel flow, i.e. $L \rightarrow \infty$, both strain rates scale with $|\dot{\gamma}_{xx}| \sim H/L$ and consequently the correction to the leading-order velocity from the variation across the plug is also $\sim H/L$.

In figure 21, we make a comparison between the predicted pseudo-plug x -velocity and that from the 2D computations. We can see that the prediction is not particularly good, in terms of the shape of the velocity profiles. It should be noted that we have not carried out a matching procedure here (Putz *et al.* 2009), which would soften the corners of the pseudo-plug x -velocity. The shape of the corrected velocity, across the pseudo-plug, does not capture the variations in the computed velocity field.

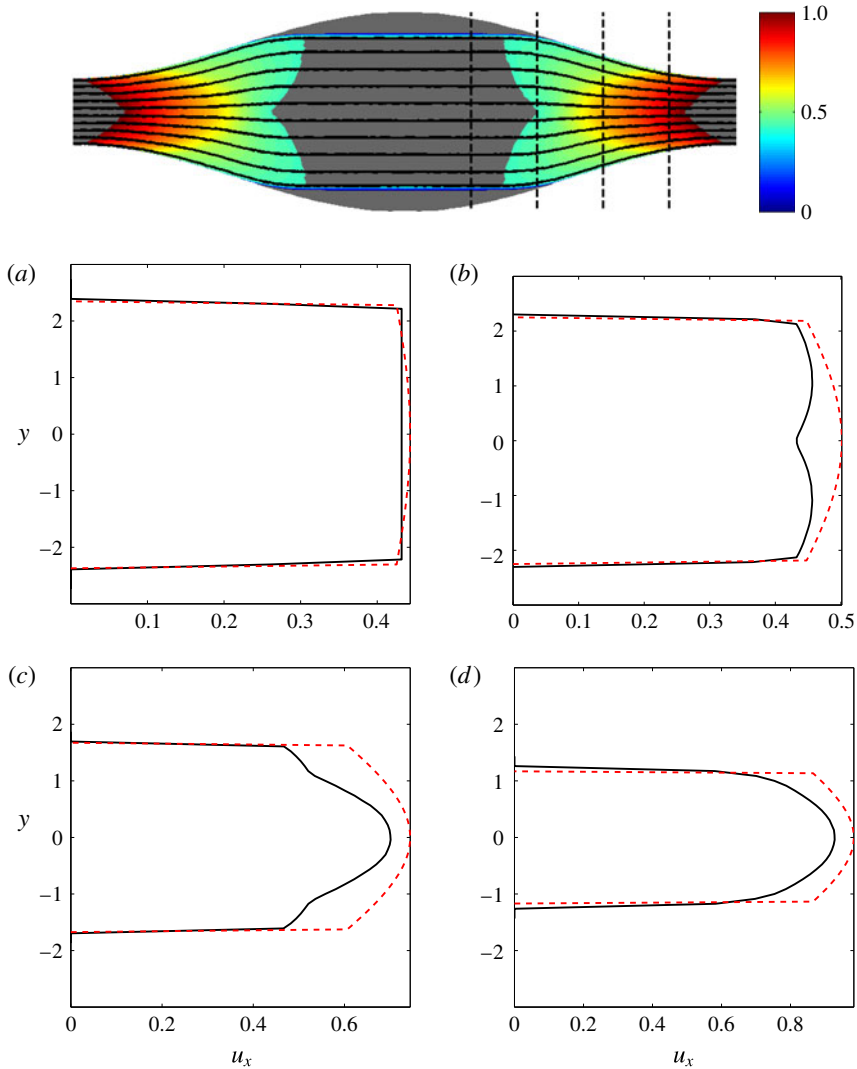


FIGURE 21. (Colour online) Comparison of the computed velocity (solid line) with the asymptotic approximation at (a) $2x/L = 0.2$, (b) $2x/L = 0.4$, (c) $2x/L = 0.6$, (d) $2x/L = 0.8$ (as marked by vertical broken lines in the colourmap). The upper figure shows the colourmap of speed with streamlines and unyielded regions in grey; $H = 2$, $L = 20$, $B = 10000$.

C.2. Pseudo-plug regions

One reason for the poor performance of the classical pseudo-plug procedure above is that the limit we consider at zero flow is the critical limit of zero flow as $B \rightarrow \infty$, for reasonably large L . However, it is not necessarily close to the asymptotic limit $L \rightarrow \infty$, which is required for the preceding analysis to be valid. The stress distribution found as $L \rightarrow \infty$ is shear-dominated, even within the pseudo-plug. Thus, for example, $\tau_{xx} \rightarrow 0$ in (C7a,b) as the yield surface is approached, as the solution must match with that in the thin shear layer close to the wall. This is not found to be the case here at intermediate L .

On the other hand, parts of the scaling of the previous section are correct. First, the velocity is observed to vanish in a relatively thin layer close to the wall. Second, since the strain rate is $\dot{\gamma} \ll B$ within the pseudo-plug, the approximation $\tau \sim B$ holds throughout the pseudo-plug. In place of (C 7a,b), the following is found to give a reasonable representation of the shear stress field within the pseudo-plug:

$$\frac{\tau_{xy}}{B} \sim -\text{sign}(y) \sqrt{1 - [f_0|h'(x)|\eta^2 + \sqrt{1 - \eta^2}]^2}, \tag{C 10}$$

$$\frac{\tau_{xx}}{B} \sim -\text{sign}(h'(x)) [f_0|h'(x)|\eta^2 + \sqrt{1 - \eta^2}], \tag{C 11}$$

where $\eta = y/(1 + h(x))$. It should be noted that $f_0 h'(x)$ approximates a normalized τ_{xx} as the walls are approached. Setting $f_0 = 0$, the distribution of (C 7a,b) is recovered, but generally we find that $f_0 \approx 1$ within the pseudo-plug. Figure 22 compares (C 11) with the computed stress distributions across the pseudo-plug for two different intermediate geometries, in both cases illustrating the good agreement.

C.3. Toy model for estimating $j(\mathbf{u})$ as $B \rightarrow \infty$

We expect that the intermediate fractures will have asymptotic behaviour as $B \rightarrow \infty$ that is intermediate between that of the short fractures and the long fractures with no fouling. Let us therefore consider fractures with relatively large L and $H \sim O(1)$ so that $h'(x)$ is relatively small. For simplicity, we consider $\psi = 0$. The flow rate constraint determines $Q(\mathbf{u}) = 2L$, and therefore to estimate Y in the limit $B \rightarrow \infty$ it suffices to estimate $j(\mathbf{u})$. We suppose that the limiting flows are divided into two distinct regions. First, in the wider part of the fracture, we assume that there are fouling layers that fill the deepest parts of the fracture for $x \in (-x_f, x_f)$. Second, for $x \notin (-x_f, x_f)$, we assume that there are no fouled regions at the walls of the fracture.

In the unfouled regions, the mean velocity in the x -direction is simply $\bar{u} = 1/(1 + h(x))$. In these regions, as we approach the walls, the velocity drops from $u \approx \bar{u}$ to zero over a thin layer of $O(B^{-1/2})$. This thin layer gives a contribution to $j(\mathbf{u})$ of approximate size

$$j_s(\mathbf{u}) \approx 4 \int_{x_f}^{L/2} \frac{1}{1 + h(x)} dx, \tag{C 12}$$

with the subscript denoting the shear layer. Further away from the wall, in the pseudo-plug, we assume that variations from the mean velocity are driven by axial variations in the fracture shape, and that $u \approx \bar{u}$. Assuming $u \approx \bar{u}$ suggests that

$$\frac{\partial u}{\partial x} \approx -\frac{h'(x)}{(1 + h(x))^2} \Rightarrow v \approx O(h'(x)), \tag{C 13}$$

and hence we expect the next order of terms approximating u to also have size $O(h'(x))$. It follows that within the pseudo-plug

$$\dot{\gamma}(\mathbf{u}) = |\dot{\gamma}_{xx}| \left[1 + \left(\frac{\dot{\gamma}_{xy}}{\dot{\gamma}_{xx}} \right)^2 \right]^{1/2} \sim \frac{2|h'(x)|}{(1 + h(x))^2} \left[1 + \left(\frac{\dot{\gamma}_{xy}}{\dot{\gamma}_{xx}} \right)^2 \right]^{1/2}. \tag{C 14}$$

The contribution to $j(\mathbf{u})$ for $x \notin (-x_f, x_f)$ within the pseudo-plug is therefore

$$j_{pp}(\mathbf{u}) \approx 4 \int_{x_f}^{L/2} \frac{2|h'(x)|}{(1 + h(x))^2} \int_0^{1+h(x)} \left[1 + \left(\frac{\dot{\gamma}_{xy}}{\dot{\gamma}_{xx}} \right)^2 \right]^{1/2} dy dx. \tag{C 15}$$

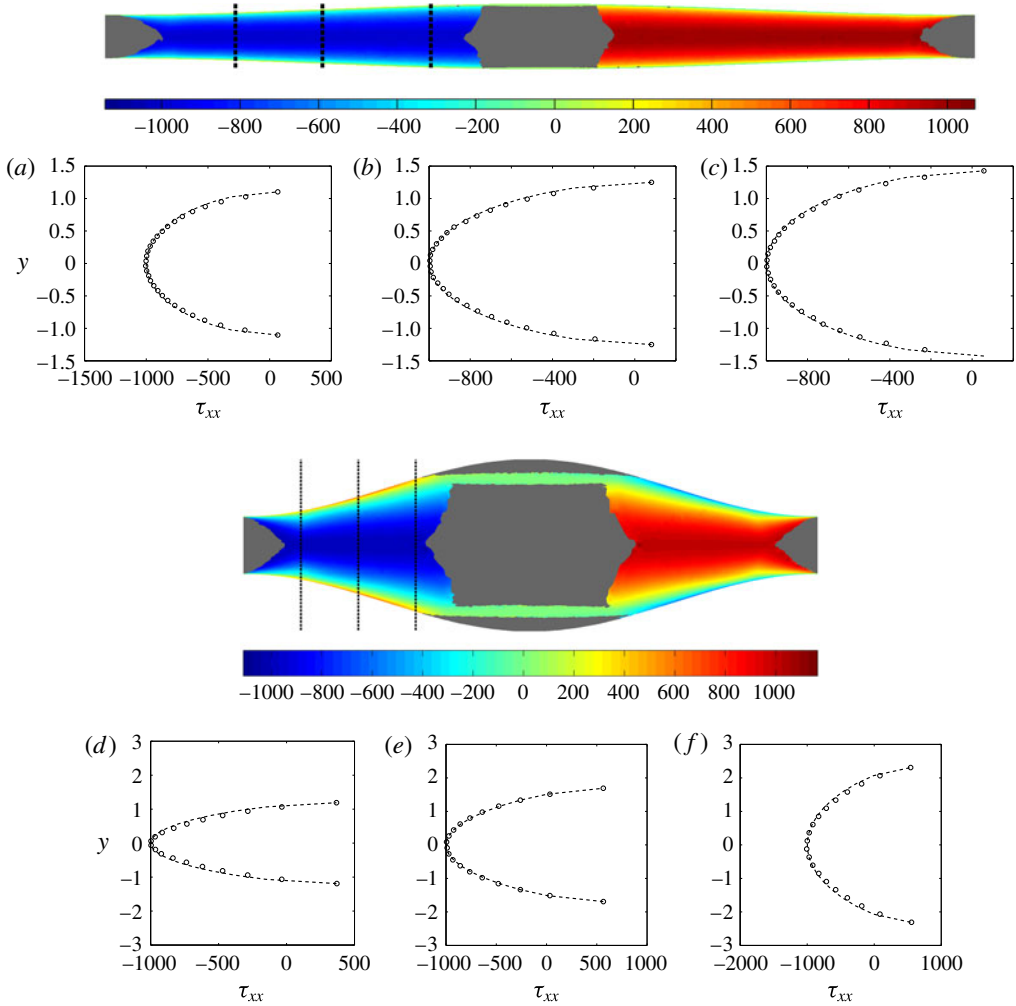


FIGURE 22. (Colour online) Colourmaps of τ_{xx} (unyielded regions in grey) for $B = 1000$. In (a–c), $H = 0.5$, $L = 40$; comparisons are shown with the predictions of (C 11) at values of $2x/L = 0.25, 0.5, 0.7$, as marked with broken lines on the colourmap. In (d–f), $H = 2$, $L = 20$; comparisons are shown with the predictions of (C 11) at values of $2x/L = 0.45, 0.6, 0.8$.

It should be noted that since we have assumed $\psi = 0$ we have exploited symmetry in both x and y to simplify this expression. To calculate the strain rates we assume that (C 10) and (C 11) approximate the stresses in the pseudo-plug. The ratio of the strain rates is then given by that of the stresses. Therefore, we find

$$\begin{aligned}
 \int_0^{1+h} \left[1 + \left(\frac{\dot{\gamma}_{xy}}{\dot{\gamma}_{xx}} \right)^2 \right]^{1/2} dy &= (1+h) \int_0^1 \frac{1}{f_0|h'|\eta^2 + \sqrt{1-\eta^2}} d\eta \\
 &= \frac{\pi}{2} \frac{1+h}{1+\sqrt{f_0|h'|}} \approx (1+h) \frac{\pi}{2} [1 + O(|h'|^{1/2})], \quad (\text{C } 16)
 \end{aligned}$$

$$j_{pp}(\mathbf{u}) \approx 4\pi \int_{x_f}^{L/2} \frac{|h'|}{(1+h)} \frac{1}{1+\sqrt{f_0|h'|}} dx = 4\pi \ln(1+h(x_f)) [1 + O(|h'|^{1/2})]. \quad (C 17)$$

Second, we consider $x \in (-x_f, x_f)$, where only a thin layer of fluid is sheared. The contribution $j_f(\mathbf{u})$ to $j(\mathbf{u})$ from the fouling region comes from the thin shear layers, at $y \approx \pm[1+h(x_f)]$. The plug velocity is approximately $u_p \approx [1+h(x_f)]^{-1}$, and it therefore follows that

$$j_f(\mathbf{u}) \approx \frac{4x_f}{1+h(x_f)} [1 + O((d'_0)^2)], \quad (C 18)$$

where again $d_0(x, B)$ is taken to represent the width of the sheared layer (see the analysis of the short fracture). To summarize, if x_f is known, then $j(\mathbf{u})$ is approximately

$$j(\mathbf{u}) \approx j_s(\mathbf{u}) + j_{pp}(\mathbf{u}) + j_f(\mathbf{u}) \\ \approx 4 \int_{x_f}^{L/2} \frac{1}{1+h(x)} dx + 4\pi \ln(1+h(x_f)) + \frac{4x_f}{1+h(x_f)} + \dots, \quad (C 19)$$

where the additional terms are of smaller order in either $1/L$ or $1/B$. Consequently, as $B \rightarrow \infty$ we approximate

$$Y(x_f) \sim \frac{Q(\mathbf{u})}{j(\mathbf{u})} \approx \frac{L/2}{\int_{x_f}^{L/2} \frac{1}{1+h(x)} dx + \frac{x_f}{1+h(x_f)} + \pi \ln(1+h(x_f))}, \quad (C 20)$$

which is (4.17), given earlier. In general, we expect that the strain rate will be minimized, among all constraints. If we regard x_f as being selected in this way, the actual x_f is determined by maximizing $Y(x_f)$ with respect to x_f , thus giving Y_c .

We have computed Y_c from this toy model, by maximizing (4.17) over x_f . Figures 23(a) and 23(b) plot respectively Y_c and x_f as functions of (H, L) . We see that the limiting behaviour for both short and very long fractures is represented in Y_c . As (H, L) both increase, the predicted Y_c also increases away from 1. The computed values of x_f are close to $L/2$ for short fractures and approach zero only for very long fractures (figure 23b). Figure 23(c) presents a contour plot of the largest value of Y attained in our computations at each (H, L) (typically computed for $B = 10^4$), which may be regarded as a computed estimate of Y_c . Comparing with figure 23(a), we see that the qualitative trends are extremely well represented by this approximation and the quantitative agreement is good for either smaller H or smaller L , but deteriorates as both parameters increase. This is, of course, not surprising, as the approximation is based on the strain rates being driven mostly by variation in \bar{u} with x , and we have neglected correction terms involving $f_0|h'|$ (valid for large L). Figure 23(d) plots the relative error between the computed Y_c from our 2D computed results and that approximated from maximizing (4.17). We see that the relative error is $< 10\%$ close to the axes and increases to approximately 15% over much of the (H, L) parameter space explored. Evidently, once both H and L are much larger than 1, the geometry represents a large vacuous space rather than a fracture.

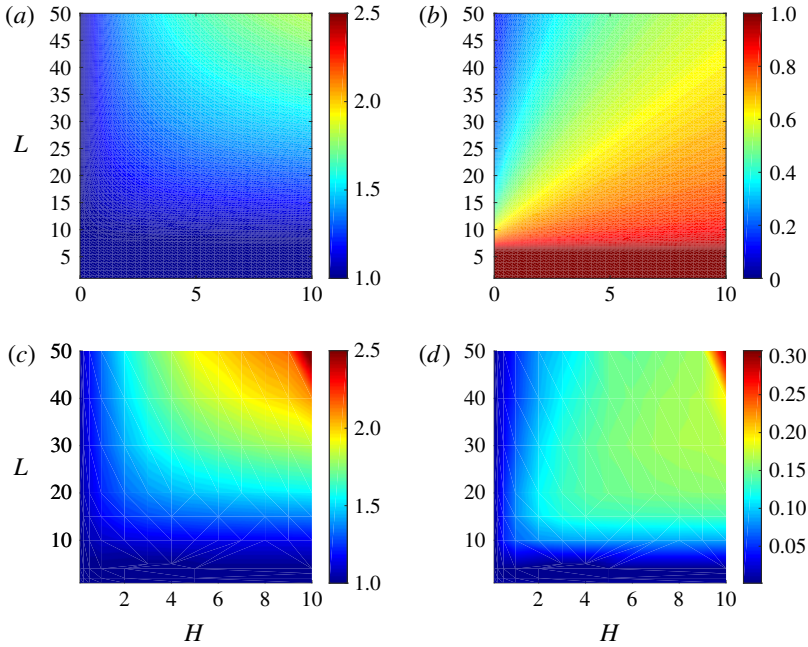


FIGURE 23. (Colour online) (a) Variation of Y_c computed by maximizing (4.17). (b) Variation of the value of x_f that maximizes (4.17), scaled with $L/2$. (c) Variation of Y_c approximated as the largest value of Y from our 2D computations, typically at $B = 10^4$. (d) Absolute relative error between (a) and (c).

C.4. An improved toy model

It is possible to improve the estimate of $j(\mathbf{u})$. From consideration of figure 21 and similar, it is evident that the pseudo-plug behaviour is more complex than that given by the proposed $j_{pp}(\mathbf{u})$. The simplest improvement is to include the neglected $f_0|h'|$ term, i.e.

$$j_{pp}(\mathbf{u}) \approx 4\pi \int_{x_f}^{L/2} \frac{|h'|}{(1+h)} \frac{1}{1+\sqrt{f_0|h'|}} dx. \tag{C 21}$$

The stress approximations (C 10) and (C 11) can be matched with the computed stresses at each x in the pseudo-plug, approximating $f_0(x)$ from the stress values close to the wall. Interestingly, this procedure suggests that $f_0(x) = \text{constant}$ throughout the pseudo-plug region. Inspection of many computations suggests that $f_0 \approx 1$.

We may now repeat the same procedure as for the toy model. We find x_f by maximizing Y_{x_f} , now defined by

$$Y(x_f) \sim \frac{Q(\mathbf{u})}{j(\mathbf{u})} \approx \frac{L/2}{\int_{x_f}^{L/2} \frac{1}{1+h(x)} dx + \frac{x_f}{1+h(x_f)} + \pi \int_{x_f}^{L/2} \frac{|h'|}{(1+h)} \frac{1}{1+\sqrt{f_0|h'|}} dx}, \tag{C 22}$$

which is (4.20), given earlier.

REFERENCES

- AL-FARISS, T. & PINDER, K. L. 1987 Flow through porous media of a shear-thinning liquid with yield stress. *Can. J. Chem. Engng* **65** (3), 391–405.
- AMBARI, A., BENHAMOU, M., ROUX, S. & GUYON, E. 1990 Distribution des tailles de pores d'un milieu poreux déterminée par l'écoulement d'un fluide à seuil. *C. R. Acad. Sci.* **311** (11), 1291–1295.
- BALHOFF, M., SANCHEZ-RIVERA, D., KWOK, A., MEHMANI, Y. & PRODANOVIĆ, M. 2012 Numerical algorithms for network modeling of yield stress and other non-Newtonian fluids in porous media. *Trans. Porous Med.* **93** (3), 363–379.
- BALHOFF, M. T. & THOMPSON, K. E. 2004 Modeling the steady flow of yield-stress fluids in packed beds. *AIChE J.* **50** (12), 3034–3048.
- BALMFORTH, N. J. & CRASTER, R. V. 1999 A consistent thin-layer theory for Bingham plastics. *J. Non-Newtonian Fluid Mech.* **84** (1), 65–81.
- BALMFORTH, N. J., FRIGAARD, I. A. & OVARLEZ, G. 2014 Yielding to stress: recent developments in viscoplastic fluid mechanics. *Annu. Rev. Fluid Mech.* **46**, 121–146.
- BARENBLATT, G. I., ENTOV, V. M. & RYZHIK, V. M. 1989 *Theory of Fluid Flows Through Natural Rocks*, Kluwer Academic.
- BITTLESTON, S. H., FERGUSON, J. & FRIGAARD, I. A. 2002 Mud removal and cement placement during primary cementing of an oil well – laminar non-Newtonian displacements in an eccentric annular Hele-Shaw cell. *J. Engng Maths* **43** (2–4), 229–253.
- BLEYER, J. & COUSSOT, P. 2014 Breakage of non-Newtonian character in flow through a porous medium: evidence from numerical simulation. *Phys. Rev. E* **89**, 063018.
- BOROUCHAKI, H., GEORGE, P. L., HECHT, F., LAUG, P. & SALTEL, E. 1997 Delaunay mesh generation governed by metric specifications. Part I. Algorithms. *Finite Elem. Anal. Des.* **25** (1–2), 61–83.
- BOUCHAUD, E. 1997 Scaling properties of cracks. *J. Phys.: Condens. Matter* **9** (21), 4319–4344.
- DE CASTRO, A. R., OMARI, A., AHMADI-SÉNICHAULT, A. & BRUNEAU, D. 2014 Toward a new method of porosimetry: principles and experiments. *Trans. Porous Med.* **101** (3), 349–364.
- CHASE, G. G. & DACHAVIJIT, P. 2003 Incompressible cake filtration of a yield stress fluid. *Sep. Sci. Technol.* **38** (4), 745–766.
- CHASE, G. G. & DACHAVIJIT, P. 2005 A correlation for yield stress fluid flow through packed beds. *Rheol. Acta* **44** (5), 495–501.
- CHEN, M., ROSSEN, W. & YORTSOS, Y. C. 2005 The flow and displacement in porous media of fluids with yield stress. *Chem. Engng Sci.* **60** (15), 4183–4202.
- CHEVALIER, T., CHEVALIER, C., CLAIN, X., DUPLA, J. C., CANOU, J., RODTS, S. & COUSSOT, P. 2013a Darcy's law for yield stress fluid flowing through a porous medium. *J. Non-Newtonian Fluid Mech.* **195**, 57–66.
- CHEVALIER, T., RODTS, S., CHATEAU, X., BOUJLEL, J., MAILLARD, M. & COUSSOT, P. 2013b Boundary layer (shear-band) in frustrated viscoplastic flows. *Europhys. Lett.* **102** (4), 48002.
- CHEVALIER, T. & TALON, L. 2015 Generalization of Darcy's law for Bingham fluids in porous media: from flow-field statistics to the flow-rate regimes. *Phys. Rev. E* **91**, 023011.
- CHRISTIANOVICH, S. A. 1940 Motion of groundwater which does not conform to Darcy's law. *Prikl. Mat. Mekh.* **4**, 33–52.
- CLAIN, X. 2010 Étude expérimentale de l'injection de fluides d'Herschel–Bulkley en milieux poreux. PhD thesis, Université Paris-Est.
- COUSSOT, P. 2005 *Rheometry of Pastes, Suspensions, and Granular Materials: Applications in Industry and Environment*. Wiley.
- COUSSOT, P. 2014 Yield stress fluid flows: a review of experimental data. *J. Non-Newtonian Fluid Mech.* **211**, 31–49.
- DRAZER, G. & KOPLIK, J. 2000 Permeability of self-affine rough fractures. *Phys. Rev. E* **62**, 8076–8085.
- DUVAUT, G. & LIONS, J. L. 1976 *Inequalities in Mechanics and Physics*. Springer.
- EL TANI, M. 2012 Grouting rock fractures with cement grout. *Rock Mech. Rock Engng* **45**, 547–561.

- ENTOV, V. M. 1967 On some two-dimensional problems of the theory of filtration with a limiting gradient. *Prikl. Mat. Mekh.* **31**, 820–833.
- FORTIN, M. & GLOWINSKI, R. 1983 *The Augmented Lagrangian Method*. North-Holland.
- FRIGAARD, I. A. & NOUAR, C. 2005 On the usage of viscosity regularisation methods for viscoplastic fluid flow computation. *J. Non-Newtonian Fluid Mech.* **127** (1), 1–26.
- FRIGAARD, I. A. & RYAN, D. P. 2004 Flow of a visco-plastic fluid in a channel of slowly varying width. *J. Non-Newtonian Fluid Mech.* **123** (1), 67–83.
- GE, S. 1997 A governing equation for fluid flow in rough fractures. *Water Resour. Res.* **33** (1), 53–61.
- GLOWINSKI, R. & LE TALLEC, P. 1989 *Augmented Lagrangian and Operator-Splitting Methods in Nonlinear Mechanics*. vol. 9. SIAM.
- HECHT, F. 2012 New development in FreeFem++. *J. Numer. Math.* **20** (3–4), 251–265.
- MALEVICH, A. E., MITYUSHEV, V. V. & ADLER, P. M. 2006 Stokes flow through a channel with wavy walls. *Acta Mech.* **182** (3–4), 151–182.
- MANDELBROT, B. B., PASSOJA, D. E. & PAULLAY, A. J. 1984 Fractal character of fracture surfaces of metals. *Nature* **308** (5961), 721–722.
- MIRZADZHANZADE, A. K. 1959 *Problems of Hydrodynamics of Viscous and Viscoplastic Fluids in Oil Drilling*. Aznefteizdat, Baku (In Russian).
- MOSOLOV, P. P. & MIASNIKOV, V. P. 1966 On stagnant flow regions of a viscous-plastic medium in pipes. *J. Appl. Math. Mech.* **30** (4), 841–854.
- MOSOLOV, P. P. & MIASNIKOV, V. P. 1967 On qualitative singularities of the flow of a viscoplastic medium in pipes. *Prikl. Mat. Mech.* **31** (3), 581–585. *J. Appl. Math. Mech.* **31** (3) 609–613.
- NELSON, E. B. & GUILLOT, D. 2006 *Well Cementing*. Schlumberger.
- PARK, H. C., HAWLEY, M. C. & BLANKS, R. F. 1973 The flow of non-Newtonian solutions through packed beds. *Polymer Engng Sci.* **15**, 761–773.
- PELIPENKO, S. & FRIGAARD, I. A. 2004 Visco-plastic fluid displacements in near-vertical narrow eccentric annuli: prediction of travelling-wave solutions and interfacial instability. *J. Fluid Mech.* **520**, 343–377.
- PUTZ, A. & FRIGAARD, I. A. 2010 Creeping flow around particles in a Bingham fluid. *J. Non-Newtonian Fluid Mech.* **165** (5), 263–280.
- PUTZ, A., FRIGAARD, I. A. & MARTINEZ, D. M. 2009 On the lubrication paradox and the use of regularisation methods for lubrication flows. *J. Non-Newtonian Fluid Mech.* **163** (1–3), 62–77.
- DE LOS REYES, J. C. & GONZÁLEZ ANDRADE, S. 2012 A combined BDF–semismooth Newton approach for time-dependent Bingham flow. *Numer. Meth. Part. Diff. Equ.* **28** (3), 834–860.
- ROUSTAEI, A. & FRIGAARD, I. A. 2013 The occurrence of fouling layers in the flow of a yield stress fluid along a wavy-walled channel. *J. Non-Newtonian Fluid Mech.* **198**, 109–124.
- ROUSTAEI, A., GOSSELIN, A. & FRIGAARD, I. A. 2015 Residual drilling mud during conditioning of uneven boreholes in primary cementing. Part 1: rheology and geometry effects in non-inertial flows. *J. Non-Newtonian Fluid Mech.* **220**, 87–98.
- ROUX, S. & HERRMANN, H. J. 1987 Disorder-induced nonlinear conductivity. *Europhys. Lett.* **4** (11), 1227.
- SAHIMI, M. 1995 *Flow and Transport in Porous Media and Fractured Rock*. VCH Verlagsgesellschaft.
- SARAMITO, P. 2016 A damped Newton algorithm for computing viscoplastic fluid flows. *J. Non-Newtonian Fluid Mech.* Available online 20 May 2016, doi:[10.1016/j.jnnfm.2016.05.007](https://doi.org/10.1016/j.jnnfm.2016.05.007).
- SARAMITO, P. & ROQUET, N. 2001 An adaptive finite element method for viscoplastic fluid flows in pipes. *Comput. Meth. Appl. Mech. Engng* **190** (40), 5391–5412.
- SAVINS, J. G. 1969 Non-Newtonian flow through porous media. *Ind. Engng Chem.* **61** (10), 18–47.
- SCHEIDEGGER, A. E. 1957 *The Physics of Flow Through Porous Media*. University of Toronto Press.
- SCHMITTBUHL, J., GENTIER, S. & ROUX, S. 1993 Field measurements of the roughness of fault surfaces. *Geophys. Res. Lett.* **20** (8), 639–641.
- SOCHI, T. & BLUNT, M. J. 2008 Pore-scale network modeling of Ellis and Herschel–Bulkley fluids. *J. Pet. Sci. Engng* **60** (2), 105–124.

- DE SOUZA MENDES, P. R., NACCACHE, M. F., VARGES, P. R. & MARCHESINI, F. H. 2007 Flow of viscoplastic liquids through axisymmetric expansions–contractions. *J. Non-Newtonian Fluid Mech.* **142** (1–3), 207–217.
- SULTANOV, B. I. 1960 Filtration of visco-plastic fluids in a porous medium. *Izv. Akad. Nauk. SSSR Ser. Fiz.* **5**, 820–833.
- TALON, L., AURADOU, H. & HANSEN, A. 2010 Permeability of self-affine aperture fields. *Phys. Rev. E* **82**, 046108.
- TALON, L., AURADOU, H. & HANSEN, A. 2014 Effective rheology of Bingham fluids in a rough channel. *Front. Phys.* **2**, 24.
- TALON, L., AURADOU, H., PESSEL, M. & HANSEN, A. 2013 Geometry of optimal path hierarchies. *Eur. Phys. Lett.* **103** (3), 30003.
- TALON, L. & BAUER, D. 2013 On the determination of a generalized Darcy equation for yield-stress fluid in porous media using a lattice-Boltzmann TRT scheme. *Eur. Phys. J. E* **36** (12), 1–10.
- TRESKATIS, T., MOYERS-GONZALEZ, M. A. & PRICE, C. J. 2015 A trust-region SQP method for the numerical approximation of viscoplastic fluid flow. Preprint, [arXiv:1504.08057](https://arxiv.org/abs/1504.08057).
- WALTON, I. C. & BITTLESTON, S. H. 1991 The axial flow of a Bingham plastic in a narrow eccentric annulus. *J. Fluid Mech.* **222**, 39–60.
- WANG, Y. 1997 Finite element analysis of the duct flow of Bingham plastic fluids: an application of the variational inequality. *Intl J. Numer. Meth. Fluids* **25** (9), 1025–1042.
- ZIMMERMAN, R. W., KUMAR, S. & BODVARSSON, G. S. 1991 Lubrication theory analysis of the permeability of rough-walled fractures. *Intl J. Rock Mech. Min.* **28** (4), 325–331.